



S velocity variations beneath North America

Heather Bedle^{1,2} and Suzan van der Lee¹

Received 23 July 2008; revised 11 February 2009; accepted 6 May 2009; published 22 July 2009.

[1] We investigate *S* velocity variation in the upper mantle beneath North America to better understand the effects of data heterogeneity, model parameterization, and regularization. To this end, we analyzed and fit regional *S* and Rayleigh wave trains generated by earthquakes around North America that occurred between the years 2000 through 2006, including waveforms from the Transportable Array stations of EarthScope's USArray. These new data were combined with constraints used for the 3-D *S* velocity model NA04 in order to create a new model, NA07. Another model, NA07, was created from a suite of good-fit models to provide a useful guide for model velocities and uncertainties by estimating ranges of probable velocity variations throughout the upper mantle. We find that the southern and eastern edges of the North American craton appear to be defined by Paleozoic orogens rather than Proterozoic ones. On average, the Archean portion of the craton is ~ 200 km thick, while the Paleozoic part averages ~ 175 km thick with an ~ 80 m/s lower *S* velocity. The horizontal gradients in velocity are over $\sim 1.0\%/100$ km at the western margin of the craton, $\sim 0.5\%/100$ km in the south, and $\sim 1\%/100$ km at the eastern margin.

Citation: Bedle, H., and S. van der Lee (2009), *S* velocity variations beneath North America, *J. Geophys. Res.*, 114, B07308, doi:10.1029/2008JB005949.

1. Introduction

[2] North America is a mosaic of geologic provinces, and while it is well studied, questions remain unanswered concerning its evolution. With the implementation of continental-scale geologic initiatives such as EarthScope's USArray, a plethora of new data is being introduced to the scientific community. In this study, we create an up-to-date framework on which future USArray analyses can build. Specifically, we update a previous 3-D *S* velocity tomographic model NA04 [van der Lee and Frederiksen, 2005], using earthquakes recorded between 2000 and 2006 by regional predecessor networks of USArray and the USArray network (Table 1) and explore model uncertainties.

[3] This study also assesses the variability between tomographic solutions to demonstrate the importance of understanding model uncertainty. Understanding variability is essential when making geologic and tectonic interpretations that rely on the propagation velocity of *S* waves in the crust and upper mantle, since velocity is proportional to the compositional, mineralogical, and thermal states of the mantle. It is crucial to quantify even minor velocity variations when interpreting *S* velocities, as, for example, a relatively small velocity increase of 1% in the uppermost mantle can be

attributed to a 5 unit increase in the Mg# relative to Fe, or an 220°C decrease in temperature at STP [Lee, 2003].

1.1. North America Tectonic Overview

[4] The North American plate is a complex tectonic region (Figure 1). Since the mid-Proterozoic, the majority of the central and eastern North American continent has been relatively stable. The widely studied western portion of the continent is an actively deforming broad region extending up to 1500 km eastward of the western North American plate boundary, which encompasses a wide range of tectonic environments.

[5] Most of the earthquakes used in this study occur at the North American plate boundaries (Figure 2). The most distinguishing topographic feature of the North American continent is the Rocky Mountain Cordillera, which extends from the far north in Alaska, through Canada, the United States and into Mexico. This mountain belt extends to and abuts the North American craton, and is marked by a very sharp contrast both topographically and as imaged by seismic velocity studies [Woodhouse and Dziewonski, 1984; Grand, 1994; Lee and Grand, 1996; van der Lee and Nolet, 1997; Laske and Masters, 1998; Li and Romanowicz, 1996; Boschi and Ekström, 2002; Grand, 2002; Godey et al., 2003; van der Lee and Frederiksen, 2005; Marone and Romanowicz, 2007]. At the center of the North American craton is the Laurentia composite craton, which is composed of several Archean cratons, among them the Slave, Rae, Hearne, Superior and Wyoming cratons [Bleeker, 2003]. These Archean cratons are believed to have amalgamated in the Proterozoic, with additional terranes (the Yavapai and Mazatzal) accreting to the margins in the west and south

¹Department of Earth and Planetary Sciences, Northwestern University, Evanston, Illinois, USA.

²Now at Chevron North America Exploration and Production Company, Covington, Louisiana, USA.

Table 1. List of Seismograph Networks

Network	Network Code
Global Seismograph Network (GSN)	IU
Cooperative New Madrid Seismic Network (NMSN)	NM
USArray Transportable Array Network	TA
United States National Seismic Network (USNSN)	US
ANZA Regional Network (ANZA)	AZ
Berkeley Digital Seismograph Network (BDSN)	BK
Caltech Regional Seismic Network	CI
Florida to Edmonton Seismic Experiment (FLED)	XR
Continental Dynamics–Rocky Mountain Project (CDROM)	XK99
Rio Grande Seismic Transect (LaRISTRA)	XM99
PEPP-Indiana Network (PEPP)	PN
Lamont-Doherty Cooperative Seismographic Network	LD
South Carolina Earth Physics Project (SCEPP)	SP
Yellowstone Intermountain Seismic Array	XC00
Eastern Snake River Plain Experiment	XJ00
Pacific Northwest Regional Seismic Network	UW
University of Oregon Regional Network	UO
NARS-Baja Seismic Array (NARS)	NR
Canadian National Seismograph Network (CNSN)	CN
Portable Observatories for Lithospheric Analysis and Research Investigating Seismicity (POLARIS)	PO
Adirondack Broadband Array (ABBA)	XJ95
North American Mantle Anisotropy and Discontinuity experiment (NOMAD)	XO97

[Karlstrom and Humphreys, 1998]. To the east of the North American craton lays the Appalachian mountain belt, formed during the formation of Pangaea in the Paleozoic.

1.2. Nonuniqueness in Tomographic Models

[6] Tomographic models differ from one another because they are derived from different data and because they are the nonunique solutions to mixed determined sets of linear equations. In addition, the use of regularization parameters (e.g., flattening, damping), as well as different approximations of the physical relationship between the model parameters (seismic velocity) and the observed data (waveforms), yield different tomographic models.

[7] The nonuniqueness results in a range of possible velocity models, all of which may fit the data equally well, which complicates the objective to determine which of the models is the “best model.” Therefore, it is important to quantify the variability of tomographic models, especially when these models are interpreted to infer the mineralogical, compositional, and thermal state of the upper mantle.

1.3. Previous *S* Velocity Studies

[8] The three-dimensional *S* velocity structure underneath the North American continent has been previously modeled in continental-wide [Grand, 1994; van der Lee and Nolet, 1997; Godey et al., 2003; van der Lee and Frederiksen, 2005; Marone and Romanowicz, 2007; Nettles and Dziewonski, 2008] and global-scale [Woodhouse and Dziewonski, 1984; Laske and Masters, 1998; Li and Romanowicz, 1996; Boschi and Ekström, 2002; Grand, 2002] tomographic models. Both scales of 3-D studies have their limitations. While the global models are able to image some of the dominant features within the continent, such as the tectonically active, seismically slow western margin, and the stable, cratonic, seismically high velocity interior of the continent, the global models do not image the regional variations we know exist from teleseismic tomography [Humphreys and Dueker, 1994]. With more heterogeneous ray path coverage, continental-scale models such as NA95 [van der Lee and Nolet, 1997], NA00 [van der Lee, 2002], and NA04 [van der Lee and

Frederiksen, 2005], and those of Godey et al. [2003] and Marone and Romanowicz [2007] have identified and discussed both large- and intermediate-scale features. These intermediate-scale models also have served as springboards for more in-depth tectonic studies [e.g., van der Lee and Nolet, 1997; Bunge and Grand, 2000; Goes and van der Lee,

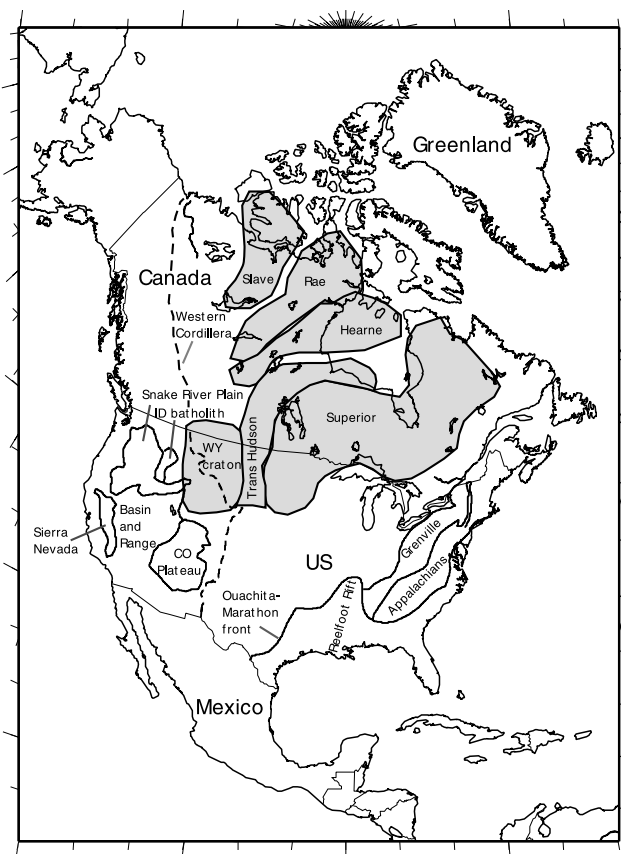


Figure 1. Map of North American geological and tectonic provinces regions discussed herein. Archean craton locations from Bleeker [2003].

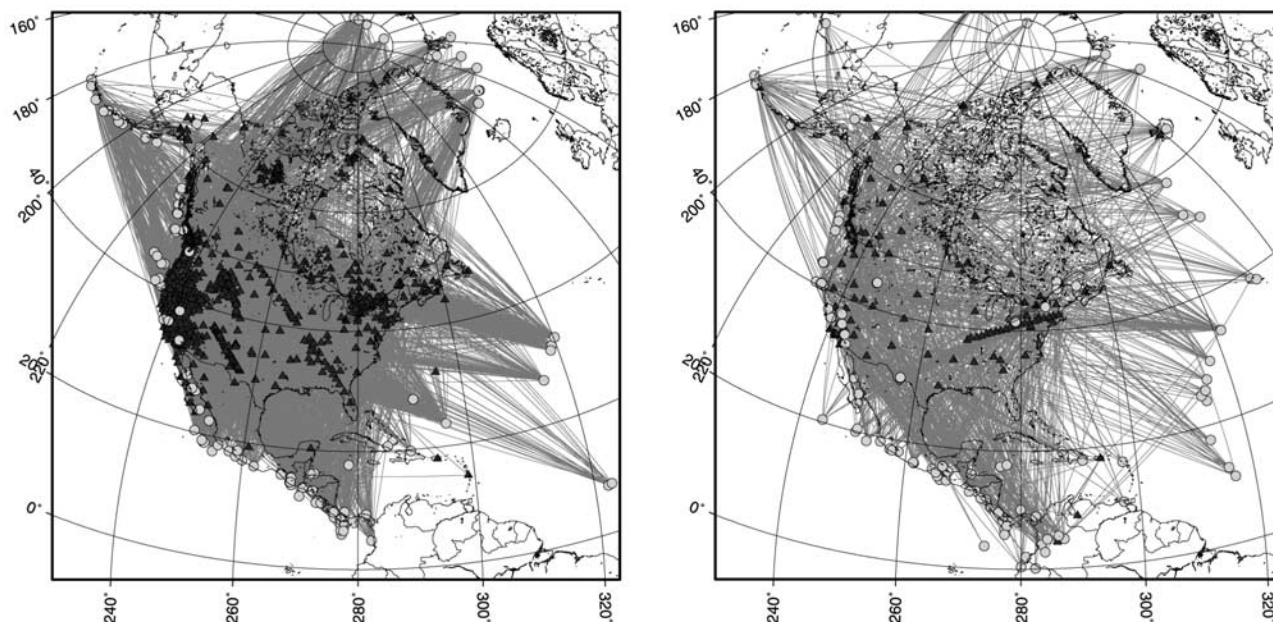


Figure 2. (left) Event-station paths for new waveforms fit in this study. Events used in this study are shown as circles. (right) Great circle ray paths for model NA04 [van der Lee and Frederiksen, 2005]. The triangles are seismic stations from which data were used in this study. Black lines connecting the events and stations represent the raypaths for data used.

2002; Menke and Levin, 2002; Schmid et al., 2002; van der Lee, 2002; Li et al., 2003; Aktas and Eaton, 2006; Bedle and van der Lee, 2006; Eaton and Frederiksen, 2007].

[9] Multiple local V_p and V_s models have also been created in recent years. These are primarily generated by teleseismic tomography using closely spaced linear arrays such as CD-ROM [Levander et al., 2005; Yuan and Dueker, 2005], RISTRA [West et al., 2004; Gao et al., 2004; Wilson et al., 2005], and DeepProbe [Gorman et al., 2002], among others. These models are impressive in lateral resolution, but provide only relative velocities for a typically two-dimensional swath, and may not have the same depth resolution as more regional studies. Future inversions that fold the results of these 2-D studies into 3-D continental-scale models should provide outstanding imaging and understanding of smaller-scale (<500 km) uppermost mantle heterogeneities.

2. Data

[10] Vertical component seismograms for regional station-event pairs for which the great circle ray path traverses the North American continent were collected (Figure 2). In this study, 5549 waveforms from 108 events (Table 2) were analyzed. The events occurred from January 2000 through September 2006, although several events from previous years were incorporated to take advantage of data recorded by the Adirondack Broadband Array (ABBA) and the North American Mantle Anisotropy and Discontinuity experiment (NOMAD), as well as to include more events in the Arctic to improve coverage of the Canadian upper mantle. Data from multiple other seismic networks were also incorporated (Table 1).

[11] This new waveform data set is entirely independent of the seismic data used in the S velocity model NA04 [van der Lee and Frederiksen, 2005]. A comparison of wave path coverage for the new data and NA04 is shown in Figure 2. The new seismic data was collected from the Incorporated Research Institutions for Seismology (IRIS), as well as from the Canadian National Data Centre for Earthquake Seismology and Nuclear Explosion Monitoring (CNDC). The earthquake source parameters were taken from the USGS National Earthquake Information Center (NEIC) hypocenter catalogue, and from Harvard's Centroid Moment Tensor Solution (CMT) [Dziewonski et al., 1983]. The origin time, latitude and longitude was acquired from the International Seismological Center (ISC), when available. In cases the ISC had not yet published origin times and locations, this information was obtained from the NEIC. After retrieval, each instrument response was deconvolved from the seismogram and checked for quality. A time window was interactively set for each seismogram so that both the fundamental and higher-mode waveforms would be fit, and strong scattered energy excluded. In some cases, separate, partially overlapping windows were set in order to focus on different frequency content within the waveform.

[12] In addition to the fixed point Moho constraints used by van der Lee and Frederiksen [2005], we incorporated crustal thickness estimates from the automated receiver functions of the EarthScope Automated Receiver Survey (EARS) [Crotwell and Owens, 2005]. EARS employs the deconvolution technique of Ligorria and Ammon [1999] and the H - κ stacking technique of Zhu and Kanamori [2000]. Although individual weighting is assigned to each of these fixed point Moho constraints, for further confidence all stations for which the crustal thickness standard devia-

Table 2. List of Events^a

Date (YYMMDD)	Time (UT)	Latitude	Longitude	Mb	Ms
950531	1608:42.50	19.050	-107.570	5.4	6.1
970706	2013:34.00	16.073	-88.095	5.5	5.5
980110	0820:10.12	14.402	-91.574	6.1	6.2
980303	0224:45.05	14.385	-91.480	5.5	5.4
980321	1633:18.80	79.840	1.580	5.9	6.1
981228	0723:32.05	20.795	-74.673	5.6	5.3
990321	1524:05.40	85.640	83.740	5.4	5.1
990607	1610:37.80	72.680	4.360	5.3	5.4
990701	0207:03.90	70.160	-14.360	4.9	5.6
000120	0941:53.49	43.697	-126.564	5.7	5.6
000203	1553:16.70	75.160	9.450	5.5	5.0
000226	1824:41.60	9.436	-78.643	5.8	5.6
000316	1519:57.78	40.404	-124.912	5.4	5.6
000521	1958:47.58	71.191	-8.222	5.3	5.5
000602	1113:49.08	44.430	-130.180	5.8	6.0
000809	1141:44.31	18.162	-102.577	6.1	6.5
001005	1339:12.59	31.891	-40.924	5.4	6.1
001212	0526:46.29	6.028	-82.660	5.8	5.7
010111	0004:06.74	49.165	-128.898	5.4	5.8
010123	0523:34.83	13.937	-91.329	5.5	5.3
010201	1819:30.98	51.429	-177.793	5.6	5.6
010213	1422:05.95	13.699	-88.874	5.5	6.4
010217	2011:30.84	53.974	-133.756	5.4	5.9
010228	1854:31.77	47.150	-122.628	6.4	6.6
010417	2154:02.96	51.200	-179.787	5.7	5.5
010626	1405:37.38	61.506	-140.022	5.8	5.4
010719	1800:40.47	57.184	-151.074	5.7	5.5
010825	0202:00.04	7.601	-82.794	5.9	5.8
010914	0445:12.05	48.913	-128.261	5.4	5.8
011008	0339:18.51	17.049	-100.069	5.6	5.4
011012	0502:35.33	52.709	-132.179	5.6	5.7
011109	0047:57.42	9.812	-82.209	6.0	5.7
011113	0947:35.02	22.383	-106.954	5.4	5.8
011128	1432:33.68	15.679	-93.129	5.6	5.7
011213	1350:46.84	27.054	-44.496	5.4	5.5
011220	1113:51.40	54.225	-162.584	5.6	5.2
020112	0826:53.29	28.323	-69.580	5.6	4.9
020116	2309:52.33	15.541	-93.134	5.8	5.7
020503	1120:55.00	86.020	31.540	5.2	5.6
020616	0246:16.26	8.921	-83.956	5.3	6.1
020709	1840:35.68	43.512	-127.188	5.4	5.5
020807	2359:14.84	7.854	-82.227	5.6	5.7
021103	0149:28.84	51.508	-130.567	5.3	5.5
021126	0048:16.79	51.494	-173.524	5.8	5.9
021023	1127:20.13	63.555	-148.068	5.9	6.7
030116	0053:15.38	44.212	-129.047	5.2	5.9
030312	2341:33.90	26.649	-110.578	5.4	6.4
030411	0612:52.98	6.997	-82.356	5.6	5.7
030519	1627:11.10	17.625	-105.469	5.5	5.9
030619	1259:23.14	71.082	-7.643	5.6	5.0
030704	0716:47.80	76.550	23.810	5.7	5.1
030712	2301:39.77	54.775	-134.346	5.3	5.6
030922	0445:36.24	19.777	-70.673	6.1	6.6
031105	0058:51.11	4.973	-77.770	5.7	5.7
031112	0454:56.42	28.967	-113.219	5.5	5.4
031222	1915:56.00	35.750	-121.150	6.1	6.5
040101	2331:50.05	17.488	-101.303	5.6	5.7
040116	1807:53.95	7.665	-37.659	5.8	6.0
040119	0722:54.10	84.520	105.230	5.5	5.2
040204	1159:43.46	08.516	-82.837	5.4	5.7
040218	1059:18.06	23.802	-109.062	5.4	5.6
040302	0347:22.40	11.610	-86.767	5.4	5.9
040414	2307:39.94	71.070	-7.750	5.6	5.5
040614	2254:20.17	16.362	-97.946	5.6	5.6
040628	0949:45.02	54.997	-134.530	5.9	6.8
040715	1206:51.20	49.574	-127.042	5.5	5.3
040719	0801:45.53	49.701	-126.949	5.9	6.1
040909	1633:21.74	17.759	-81.550	5.8	5.4
040918	2302:18.33	37.985	-118.638	4.4	5.0
040924	1443:09.69	28.677	-112.877	5.5	5.7
040928	1715:24.54	35.854	-120.092	4.9	5.8
041009	2126:53.70	11.250	-87.020	6.6	5.6
041102	1002:10.74	49.234	-128.838	5.1	6.5

Table 2. (continued)

Date (YYMMDD)	Time (UT)	Latitude	Longitude	Mb	Ms
041120	0807:22.73	9.726	-84.051	5.3	6.3
041213	1523:42.40	13.671	-89.272	5.0	5.5
050228	0105:59.30	18.760	-104.590	5.5	5.5
050306	0521:44.60	84.930	98.690	6.1	6.1
050315	0015:25.00	11.240	-86.070	5.5	5.5
050317	1337:37.11	15.140	-91.380	5.1	5.7
050402	1252:36.59	78.610	6.100	5.5	5.8
050409	1516:27.89	56.170	-154.520	5.8	5.7
050508	1707:35.77	20.350	-109.190	5.5	5.5
050609	1400:49.90	51.550	-131.120	5.2	5.5
050612	1541:45.54	33.530	-116.570	5.6	5.6
050615	0250:53.18	41.300	-125.970	6.2	7.1
050617	0621:42.28	40.770	-126.570	6.6	6.6
050627	1135:45.60	18.780	-107.300	5.8	5.9
050702	0216:43.70	11.240	-86.170	6.7	6.7
050729	0500:30.09	52.910	-168.650	5.5	5.5
050805	0056:57.30	51.160	-177.930	5.6	5.3
050923	1348:31.40	16.130	-87.490	5.9	5.4
051120	1253:06.80	53.750	-163.930	5.7	5.8
051216	1024:58.90	12.170	-89.860	5.6	5.5
051221	1432:37.12	6.708	-82.791	5.9	5.3
051230	1826:46.69	7.641	-82.157	5.8	5.4
060106	0339:58.55	6.640	-82.340	5.6	6.0
060120	0853:56.10	31.240	-41.440	5.5	5.4
060220	0656:12.60	13.240	-87.620	5.6	5.2
060404	0230:28.30	18.750	-107.100	5.4	5.9
060410	0626:18.00	7.770	-36.980	5.0	5.7
060510	0242:56.90	52.210	-169.190	6.1	6.4
060618	1828:06.90	32.970	-39.750	5.5	5.9
060729	1953:44.60	23.780	-64.010	5.5	5.8
060730	0121:01.40	26.870	-111.360	5.3	5.9
060811	1430:44.00	18.500	-101.060	6.0	6.1
060901	1204:25.40	53.880	-166.110	6.0	6.0
060620	1002:11.00	51.450	-130.740	5.2	5.6

^aYYMMDD is year, month, and day; read 950531 as 31 March 1995.

tion exceeded 5 km were discarded. Inversions for crustal thickness were run both with and without the EARS data, and it was found that differences between the two crustal thickness maps are minimal, with most of the minor variations occurring in the western United States where the majority of the EARS data was located.

3. Method: Theory

[13] To image the three-dimensional upper mantle *S* velocity structure under the North American continent, fundamental and higher-mode Rayleigh waveforms from vertical component seismograms were inverted using the method of Partitioned Waveform Inversion (PWI). For an in-depth discussion of PWI theory, we refer to *Nolet* [1990] and *van der Lee and Nolet* [1997]. Essentially, PWI derives linear constraints on the path-averaged structure along each station-event path, providing information for both the *S* velocity and Moho depth. To do this, synthetic seismograms are constructed for each path by summing the first 20 Rayleigh mode branches. The synthetics are then nonlinearly fit to the observed *S* and surface waveforms. The observed seismogram is windowed and filtered so that only the direct, unscattered portion of the waveform is used during waveform fitting. Figures 3 and 4 display the initial waveforms and the final waveforms resultant of waveform fitting. Figure 3 shows that for Event 040628 station A11, the fundamental mode arrives earlier, confirming high velocities in the upper

part of the mantle as would be expected as the wave path traverses the North American craton. For station WCI, the fundamental mode does not arrive as early, suggesting that the fast velocities are either less fast than the Archean portion of the craton as seen for station A11, or that the wave travels through less of the craton. For this event the data arrives late for both BOZ and HWUT, confirming low velocities in the western United States.

[14] Using the constraints from all selected seismograms, a regularized linear inversion was performed to retrieve a 3-D *S* velocity structure by setting up a system of linear equations, $\mathbf{G}\mathbf{m} = \mathbf{d}$, where \mathbf{G} is the constraint matrix, \mathbf{m} the model matrix, and \mathbf{d} the data vector. Because the system is partly underdetermined, regularization is applied to the inversion by adding flattening and damping equations to the system formed by the waveform and Moho constraints. The flattening parameter works by inhibiting unlikely rapid velocity variations between two neighboring grid points, while the damping parameter acts to suppress the effects of data outliers. Therefore, the data vector, \mathbf{d} , contains four different types of data: (1) path-averaged and depth-weighted *S* velocities, (2) path-averaged Moho depths, (3) zeros for damping equations, and (4) zeros for flattening equations.

[15] During the linear inversion, for which the LSQR algorithm of *Paige and Saunders* [1982] is employed, independent observations on Moho depths are used in conjunction with the waveform constraints to jointly invert and further constrain crustal thicknesses. Incorporating these

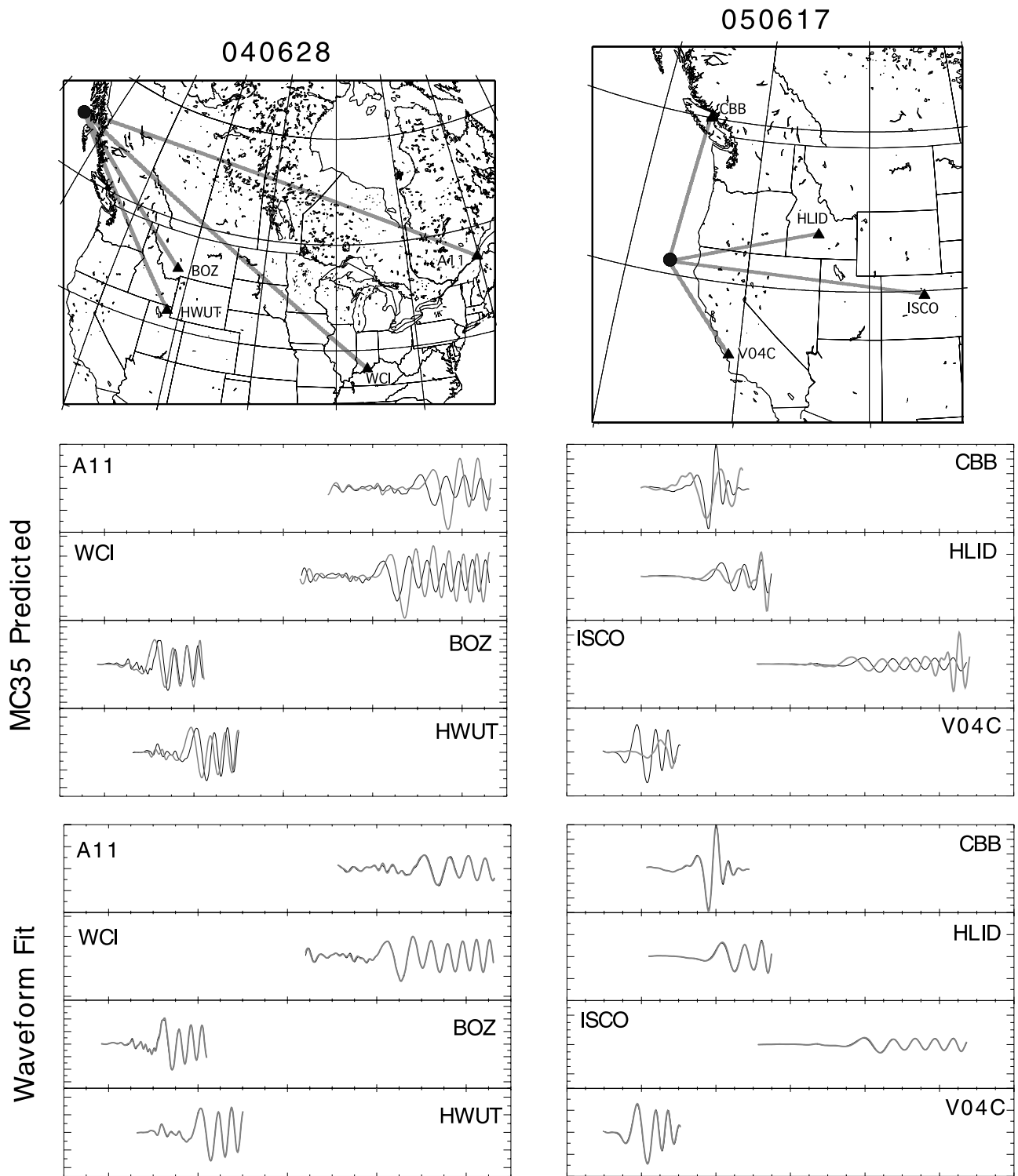


Figure 3. Waveform fits for events 040628 and 050617. The maps show the location of each event and the raypaths of the related waveforms. The observed seismograms are shown in black, and the synthetic waveform fits are shown in grey.

crustal thicknesses aids in reducing the tradeoffs between crustal thickness and uppermost mantle S velocities.

[16] The resultant 3-D model is derived relative to a 1-D reference model, MC35 [van der Lee and Nolet, 1997], which is based on PEM-C [Dziewonski et al., 1975], with

the upper mantle set to a constant S velocity of 4.5 km/s down to 210 km (Figure 14). The S velocity model uses a triangular grid of nodes, with a spacing of ~ 250 km in the horizontal direction. In addition to the Moho, nodes are placed at 24 depths in the upper mantle [0, 10, 20, 35, 50,

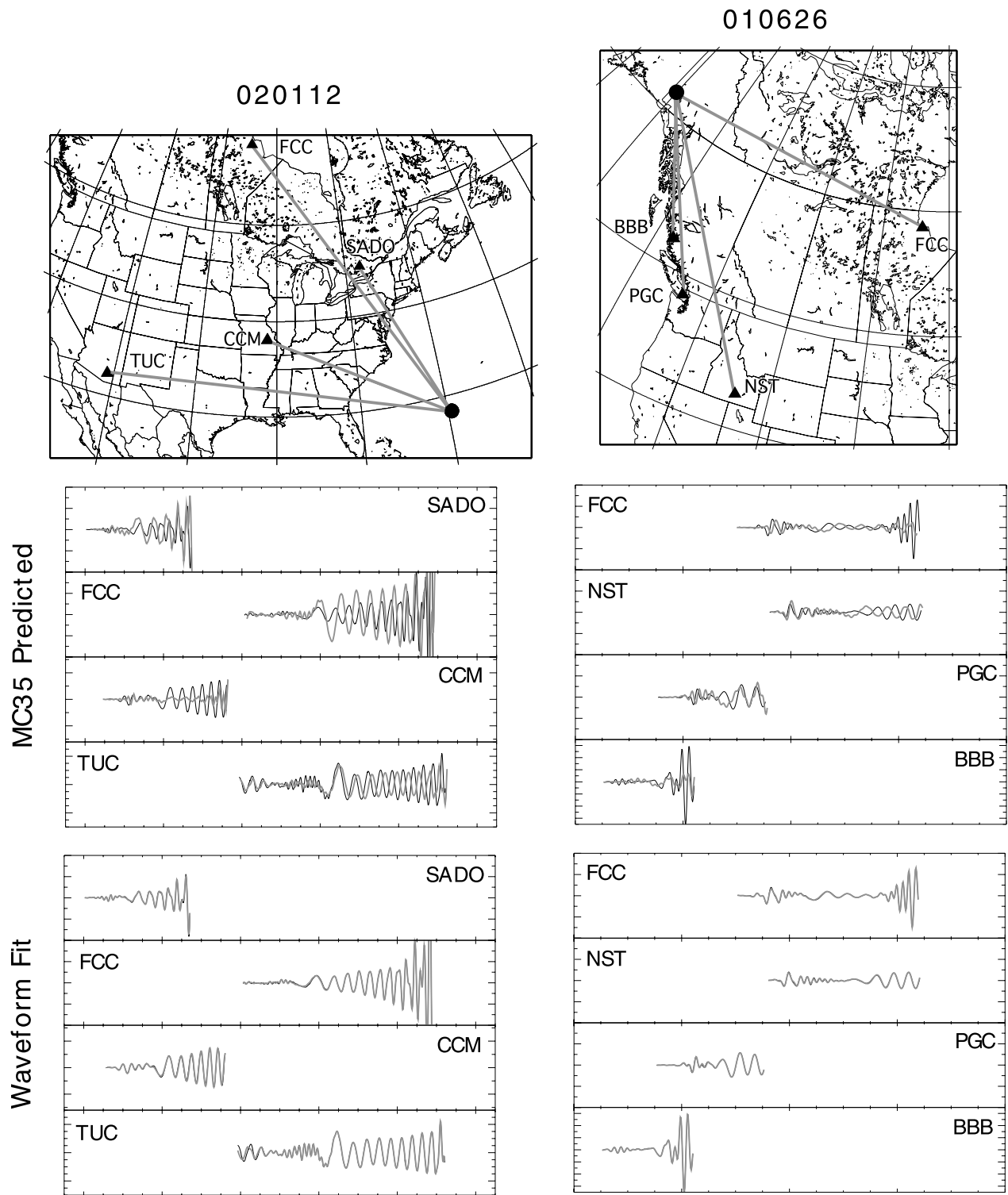


Figure 4. Waveform fits for events 020112 and 010626. The observed seismograms are shown in black, and synthetics are shown in grey.

65, 80, 95, 110, 125, 150, 175, 200, 260, 300, 350, 410, 470, 530, 590, 660, 730, and 800 km].

4. Methods: Applied

4.1. Comparison of New Data to NA04

[17] Inverting only the new set of waveform fits yields a new 3-D *S* velocity model (HB07), which is parameterized

differently than model NA04 [van der Lee and Frederiksen, 2005]. Tomographic models discussed in this text are summarized in Table 3. Although these two models use completely independent waveform data and employ different parameterization, the overall agreement of major velocity features are similar. The extent of the craton, both geographically and with depth, is similar between NA04 and HB07,

Table 3. Tomographic Models

Model	Reference	Data
NA95	<i>van der Lee and Nolet</i> [1997]	Early model of North America
NA00	<i>van der Lee</i> [2002]	NA95 data + MOMA array
NA04	<i>van der Lee and Frederiksen</i> [2005]	NA00 data + Canadian data
IL05	<i>Bedle and van der Lee</i> [2006]	NA04 + midcontinent US data
HB07	this study	2000 to 2006 North American data + ABBA and NOMAD arrays
NA07	this study	Mean model of good-fit models

although the Canadian portion of the North American craton is modeled with a higher velocity in NA04 than in HB07 down to 160 km depth. This is likely due to the waveform coverage of each of the data sets, as HB07 does not contain as many Arctic events as NA04. Resolution tests show that HB07 is not as capable of retrieving the velocity structure of the northern Slave, Rae, Hearne, and Superior cratons as model NA04, but has better resolution than NA04 beneath the United States [Bedle, 2008]. In the transition zone, HB07 images moderately higher velocities beneath the western United States, which extend further to the north and east than in NA04. Additionally, HB07 retrieves a higher-velocity seismic signature that underlies most of the western and central portions of the continent, ~2% higher than the PEM-C based averaged earth model.

4.2. Effects of Regularization

[18] To create a new North American upper mantle model, we include crustal and upper mantle constraints from the

waveform fits used in models in NA04, as well as the midcontinent data introduced in model IL05 [Bedle and van der Lee, 2006]. Incorporating these two data sets adds an additional 1433 waveforms to the new set of 5549 waveforms. This resultant new data set contains five times the number of waveforms used in NA04. The statistical distribution of waveform properties are shown in Figure 5. Figures 5b and 5c summarize the event related data. The majority of seismic waveforms were generated by strike-slip earthquakes, and were from events with Mb of 5.5 to 7.0, and Ms of 5.5 to 6.5. The lower-magnitude waveforms primarily come from the midcontinent events used previously for model IL05 [Bedle and van der Lee, 2006].

[19] Because the linear equations are partly underdetermined, we apply both flattening and damping during the inversion. In order to choose regularization parameters that allow for the optimal trade-off between data variance and model variance, several sets of inversions were run with

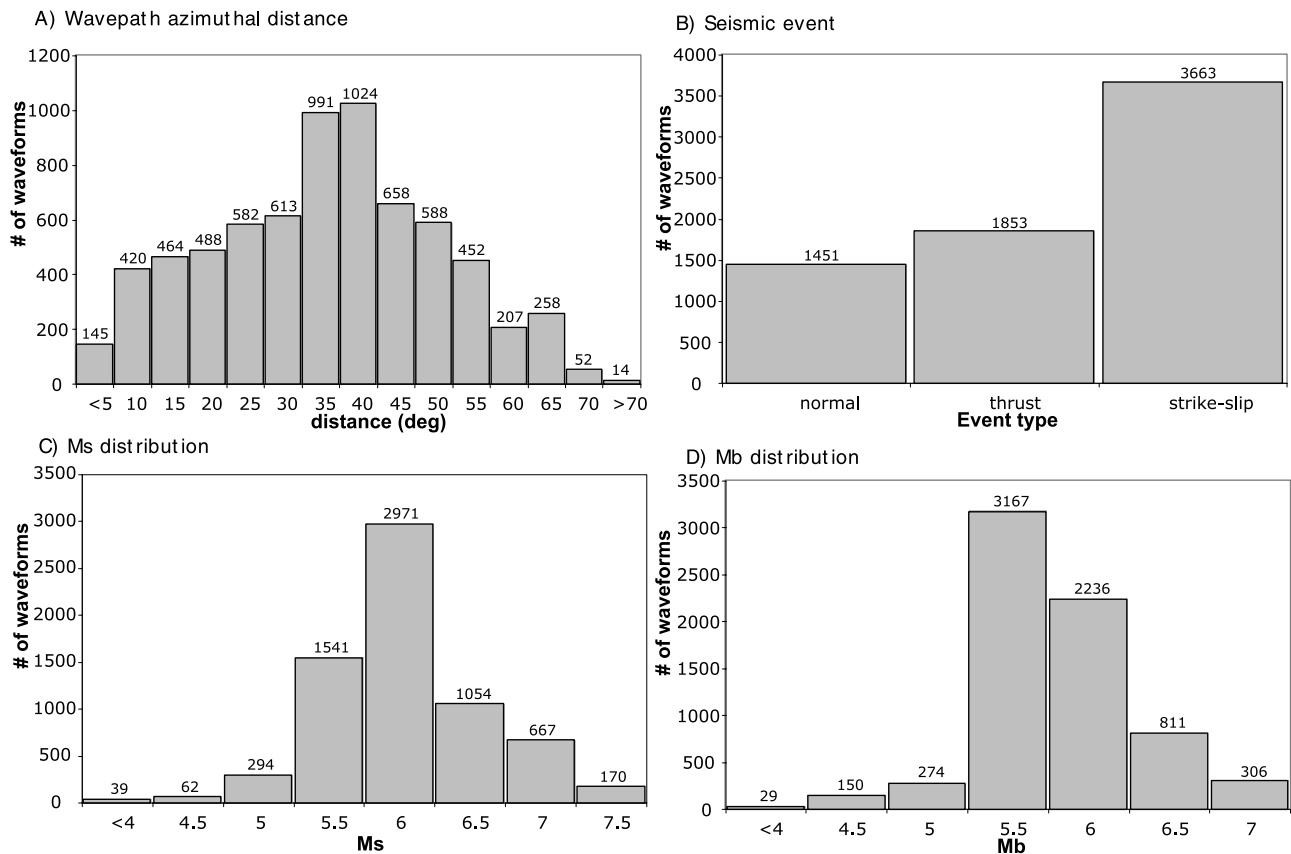


Figure 5. Histograms of waveform distribution. (a) Waveform distribution as a function of distance between event and station. (b) Tectonic regime of the even from which the waveform was generated. (c) Ms and (d) Mb distribution of the waveforms.

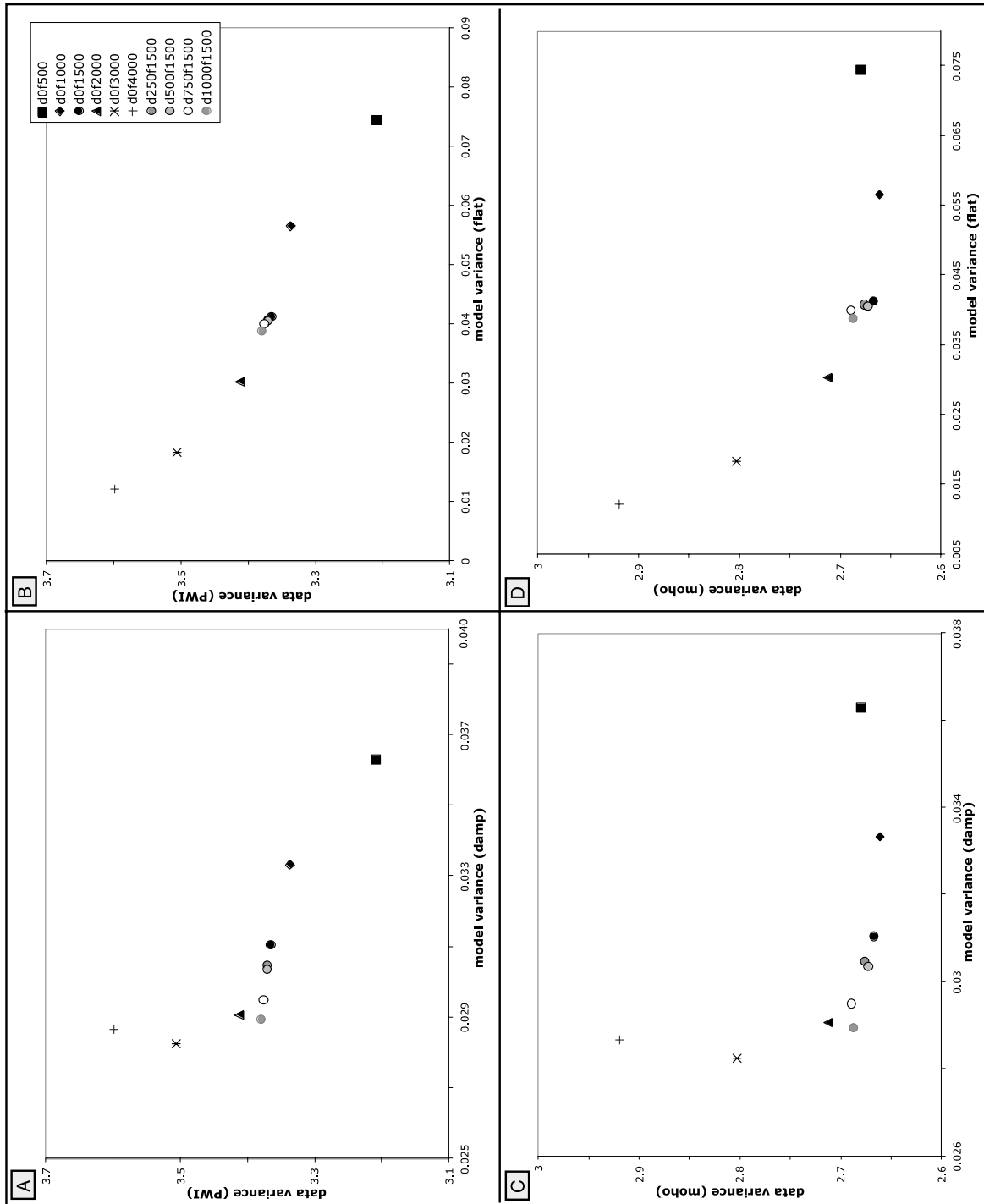


Figure 6. Data variance plotted as a function of model variance, showing the dependence on the damping and flattening parameter chosen. The plots have been normalized to one standard deviation. The key shows the amount of damping (d) and flattening (f) for each point. (a) Waveform (PWI) data misfit as a function of model damping, (b) waveform (PWI) data misfit as a function of model flattening, (c) Moho fixed point data misfit as a function of model damping, and (d) Moho fixed point data misfit as a function of model flattening.

varying smoothing parameters. Initially models were inverted for using no damping, and with the flattening parameter set to either 500, 1000, 1500, 2000, 3000, or 4000, where the larger numbers represent a higher amount of applied flattening. The data variance (RMS fit) of both the waveforms fits and the Moho fixed point constraints were plotted and compared to the damping and flattening model variance (Figure 6). We find that a flattening parameter of 1500 allows for the optimal trade-off between the model and data variances. Next, using a flattening parameter of 1500, the damping parameter was varied and we found that damping has a noticeable effect on the model and data variance. So, to take advantage of the improvement in model variance, without jeopardizing data variance, an intermediate amount of damping (250) is preferred. Resolution tests of a model with this preferred regularization shows that it neither artificially smoothes over resolvable structure (such as the Paleozoic eastern margin or the north–south variation in the stable-to-active structural transition), as occurred in models with stronger regularization, nor does it introduce small-scale artifacts into the model, as weaker regularization did in rougher models [Bedle, 2008].

4.3. Effects of Data Selection

[20] A primary source of variation in tomographic models is the choice of data. For example, the distribution of available wave paths influences the model, resampling some regions, undersampling others. In the attempt to address and quantify possible variations between models due to data choices, several model suites were created in order to estimate the statistical differences between suites of models. First, we look at the velocity differences in models created by selecting random sets of events. Secondly, we address the effects that introducing additional waveform constraints has on the resultant models by selecting random waveforms from the data set. These effects are discussed and shown in more detail by Bedle [2008].

4.3.1. Removing Events

[21] A suite of twenty tomographic models was inverted for, each with $\sim 3\%$ of the events randomly removed (events are sorted to geographic area, so no model is artificially biased by removing nearby events). The laterally averaged standard deviations in this suite of tomographic models are ≤ 6 m/s. When removing $\sim 15\%$ of the events per inversion, the standard deviation maximum at a given depth increases to 10 m/s. Overall these differences in variation amount to $\ll 1\%$ of the absolute S velocity.

[22] The mean model of the suite with $\sim 15\%$ events removed per model has minimal variance in the center of the continent. The highest variances within this suite occur along the rim of the continent, in areas where earthquake and station geometry do not allow for sufficient azimuthal coverage of wave paths.

4.3.2. Removing Random Waveforms

[23] Next, six suites of 20 models were created by randomly selecting 1000, 2000, 3000, 4000, 5000, and 6000 waveforms from the set of 6986 waveforms. We find that as more waveforms are incorporated into the inversion, the spread of RMS residual for the entire data set decreases, as discussed by Bedle [2008]. This implies that the models are beginning to approach a stable 3-D velocity structure. The converging of the 3-D velocity structure suggests that

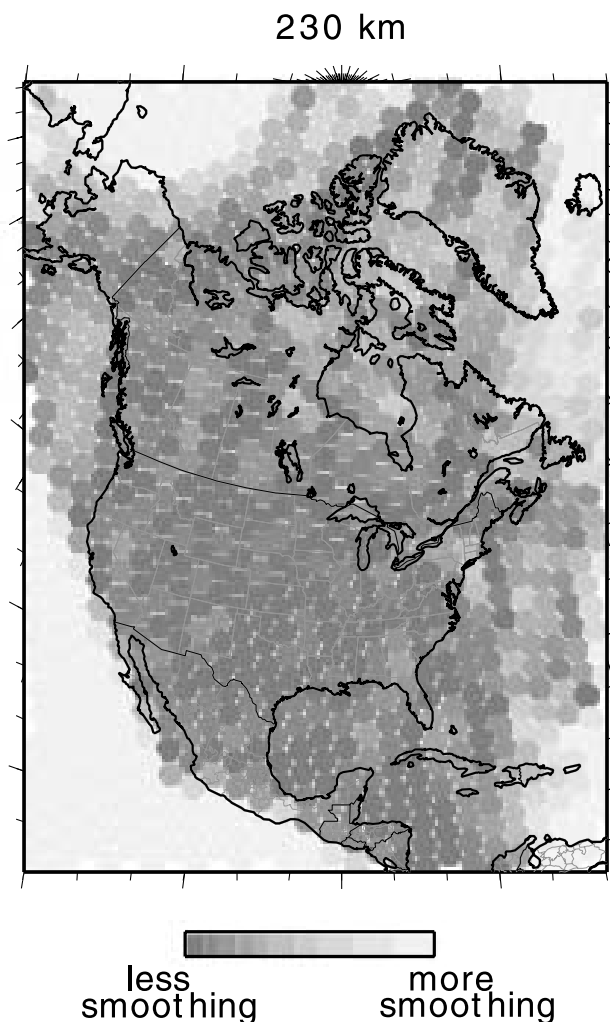


Figure 7. Smoothing parameter weighting employed at each node at 230 km depth. Darker shades represent nodes with less smoothing, and lighter colored nodes had more smoothing applied.

there is a limit to how many waveforms are needed to optimize the tomographic model with its current parameterization and data coverage. Better coverage and more data are still needed in the central, eastern, northern, and southern portions of the continent, but USArray's Transportable Array will be providing this necessary coverage over the central and eastern United States in the upcoming years.

4.4. Errors Introduced by Theory

[24] When defining the forward problem, assumptions are made concerning the relationship between model parameters and data. A choice of sensitivity kernel must be made; whether the great circle approximation is used, or if great circle path with a finite width is employed [Yoshizawa and Kennett, 2002; Ritzwoller et al., 2002], or if mode-coupling effects and wave path scattering are taken into account [Li and Romanowicz, 1996; Friederich, 2003]; as well as anisotropic considerations. In a previous study, van der Lee and Frederiksen [2005] investigated the effects that such varying sensitivity assumptions have on tomographic models

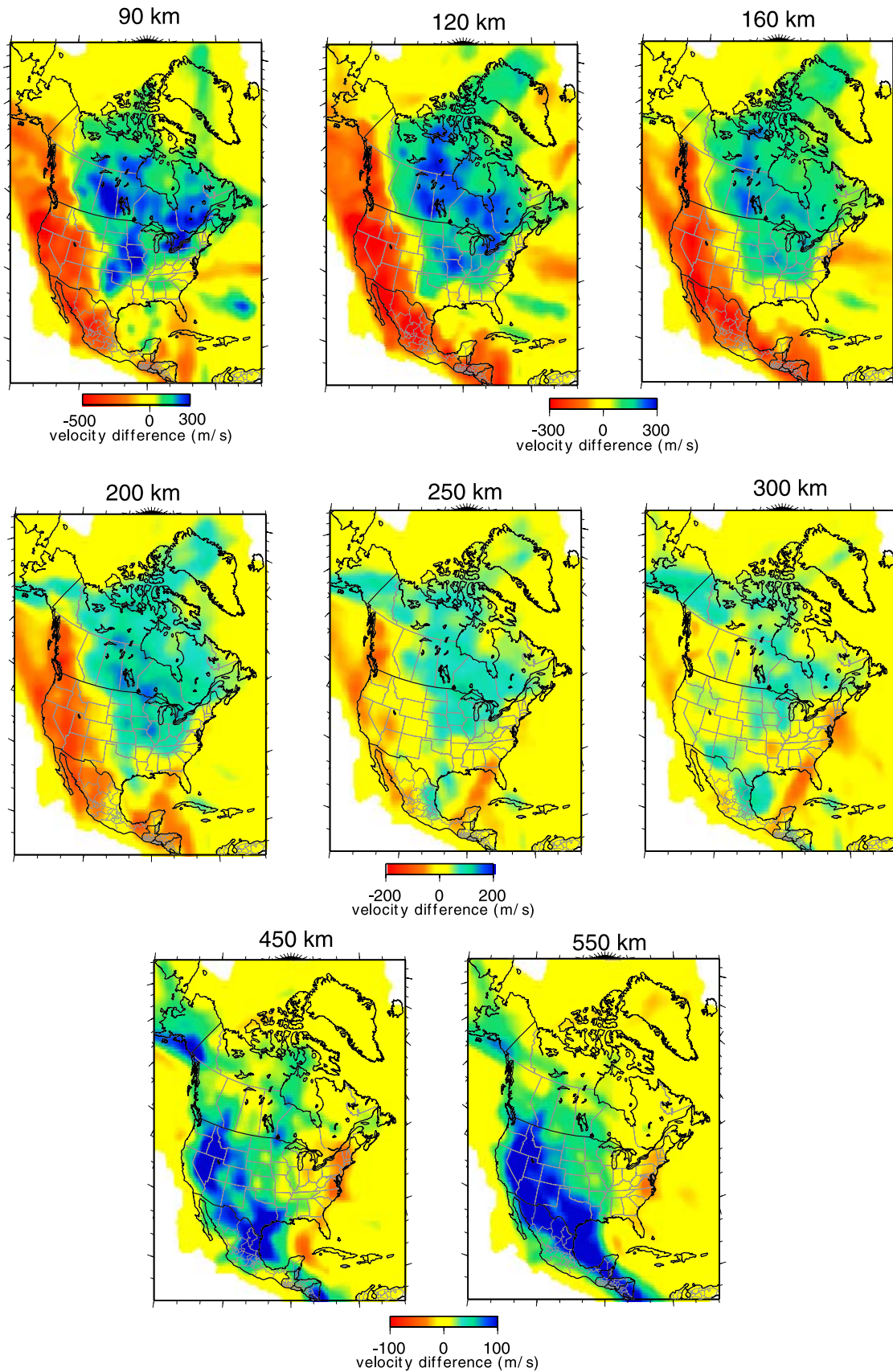


Figure 8. Horizontal depth slices through model NA07. Velocities are plotted relative to a 1-D averaged earth model. Shown are depths at 90, 120, 160, 200, 250, 300, 450, and 550 km.

and found that the effects are minimal, as compared to effects from data distribution and inversion parameterization.

[25] The effects of anisotropy on our isotropic model also need to be considered, both azimuthal and radial. Several previous studies have been conducted concerning the effects of anisotropy on tomographic models in North America [Marone and Romanowicz, 2007; Marone et al., 2007]. They modeled the azimuthal anisotropy around 2% in the uppermost mantle. On the other hand, a different study of azimuthal anisotropic bias in model NA04 show on average a 1% bias in the uppermost mantle in the worst case scenario when azimuthal anisotropy is primarily limited to the lithosphere, although in a few regions the bias can be as high as 3% [Lloyd and van der Lee, 2008]. In a recent radial anisotropy study of North America, Marone et al. [2007] modeled azimuthal bias of $\sim 1\%$ in the North American craton. The highest radial anisotropic bias in this study was modeled to be above 200 km depth, with smaller biases in the transition zone. Overall, studies suggest that anisotropic bias can introduce artificial velocity anomalies down and up to -1% and $+1\%$, respectively, averaging to near zero over large spatial scales and roughly averaging to about $|0.5\%$ on smaller, but still resolvable structural scales. Such anomalies are very small compared to the isotropic lateral heterogeneity in the North American upper mantle.

4.5. Preferred Model

[26] The path coverage of the new seismic data over the North American continent, while denser than previous models, is still not homogeneous because of earthquake and station location limitations (Figure 2). This new data set takes advantage of the increased station distribution in the United States, particularly in the western portion of the United States. Canada and Mexico have relatively good path density due to earthquake geometry, even though those regions are sampled by fewer seismic stations. Current wave path coverage predicts optimal resolution for the south central part of the continent, and not along the fringes of the continent, such as in northern Canada where stations and events are sparse. In addition, the Pacific and Atlantic oceans are not as well sampled, and the seismic waves primarily propagate parallel to one another, with minimal cross cutting of ray paths. Therefore, in these oceanic regions there is a high amount of lateral smearing along the dominant direction of seismic wave propagation, and seismic resolution is more limited. To account for this heterogeneous wave path coverage, the flattening and damping parameters are additionally scaled so that less smoothing is engaged in better resolved regions, and a greater amount of smoothing regularization is employed in regions that are not as well resolved. An example of the regularization weighting is shown at 230 km in Figure 7 and is discussed further by Bedle [2008].

4.5.1. Model NA07

[27] Using the parameterization discussed in section 4.2, along with the variable regularization weighting, we invert for the new 3-D model NA07. This new model is presented at various depths in Figure 8, as well as in cross section (Figure 9). In general, the high-velocity cratonic signature is modeled to depths of ~ 250 km, as seen in both the depth slices and in cross section. The craton extends from the Queen Elizabeth Islands in northern Canada, south and east to the Ouachita and Appalachian fronts in the United States,

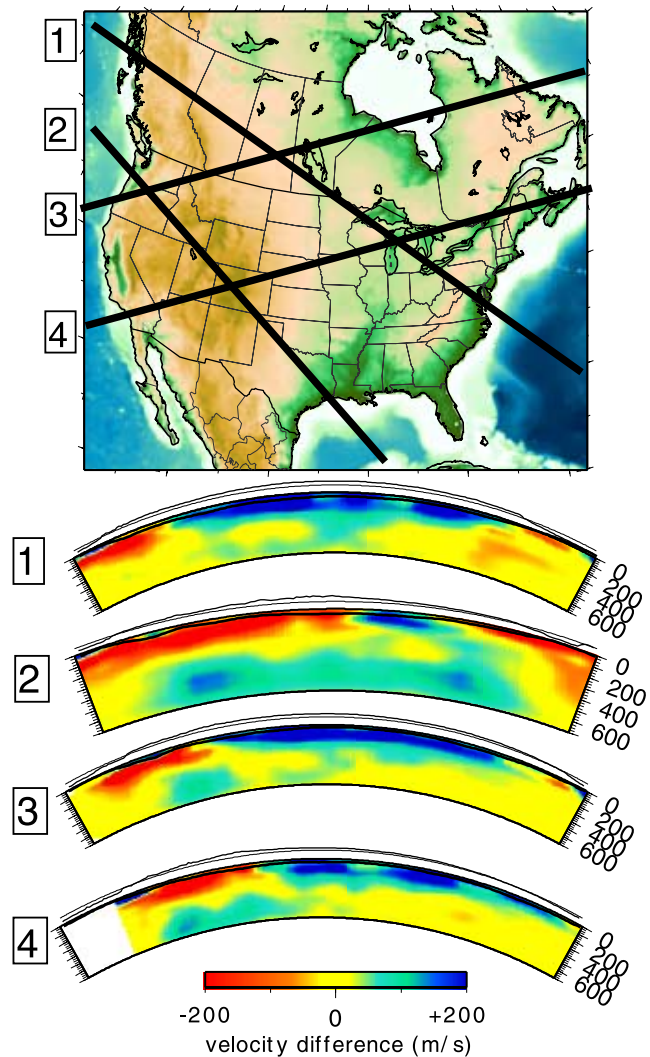


Figure 9. Cross sections through model NA07. Velocities are plotted relative to the 1-D averaged earth model. Shown are continental-scale cross sections to depths of 700 km.

and is primarily bounded in the west by the Rocky Mountain front. Smaller-scale variations within the craton are observed, notably higher-than-average velocities beneath the Hearne and Superior cratons in Canada. To the south of the North American craton, lower velocities possibly associated with the Reelfoot Rift beneath the Mississippi Embayment are retrieved. The Yucatan block of Mexico, as well as Cuba are underlain by high velocities. As expected, the asthenosphere beneath the western Cordillera has low velocities and is shallow, with the lowest-velocity regions lying beneath the Juan de Fuca and Baja spreading ridges. In the transition zone, high velocities, possibly related to subducted slabs, underlie the western and central continent, and lower velocities are found beneath the eastern seaboard.

[28] In cross section, NA07 clearly models low velocities in the asthenosphere beneath the western continent extending to depths of 200 km, although some regions are shallower, particularly beneath the Canadian portion of the cordillera (cross section 1 of Figure 9). Even within the low-velocity western asthenosphere, smaller-scale high anomalies are modeled in the uppermost mantle. The eastern portion of

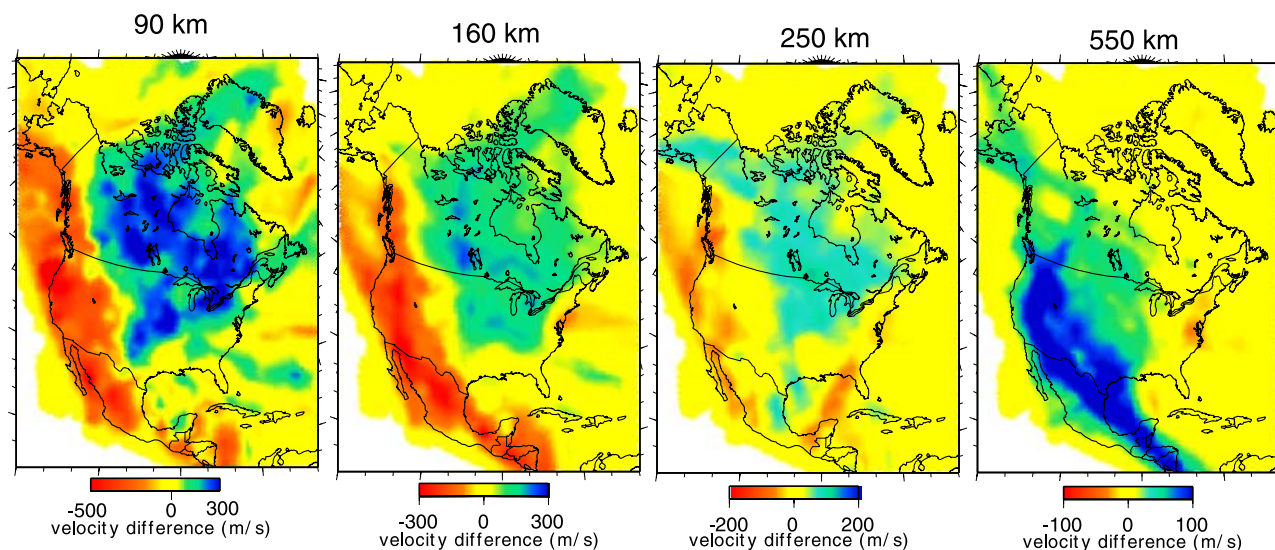


Figure 10. Depth slices at 90, 160, 250, and 550 km through model $\overline{\text{NA07}}$.

cross section 1 shows the weakly low velocities that have been previously imaged beneath the eastern continental shelf [van der Lee *et al.*, 2008]. The extent of the North American craton into central Texas is seen in cross section 2. Interestingly, the western edge of the craton appears thinner and with lower velocities in the United States (cross section 4), while it retains its thickness to the north in Canada (cross section 1). In the transition zone beneath the western United States, high velocities possibly related to the subducted Farallon slab are imaged.

4.5.2. $\overline{\text{NA07}}$

[29] To understand uncertainty, a suite of 20 tomographic models is calculated. This model suite uses the regularization weighting, flattening parameters between 1000 and 3200, damping parameters between 300 and 700, and includes a random set of 4000 or more waveforms. These ranges are chosen to encapsulate the preferred parameterization and data choices as discussed by Bedle [2008], while allowing for a preference of creating smoother models. The mean model, $\overline{\text{NA07}}$, created from this suite of good-fit models is shown in Figure 10.

[30] Overall the velocities modeled in $\overline{\text{NA07}}$ are unsurprisingly similar to model NA07. The primary differences between $\overline{\text{NA07}}$ and NA07 are the removal of some smaller-scale, features that were eliminated during the process of averaging. Robust small-scale anomalies are not removed from $\overline{\text{NA07}}$, such as high velocities to 120 km depth beneath the Yucatan Peninsula, as well as higher-velocity regions throughout the North American craton. The base of the craton remains robust, extending to depths of ~ 250 km.

4.5.3. Synthetic Resolution Tests

[31] To understand the general ability of the model to resolve large-scale velocity anomalies, a resolution test was performed using all of the data and a simplified synthetic structure consisting of the large-scale tectonic domains commonly imaged in global tomographic models. This test shows that the overall resolving power decreases with depth, particularly in the transition zone (Figure 11). Some horizontal smearing is evident in regions, such as central Canada, where ray paths tend to run parallel with minimal cross cutting (Figure 12). Within the continent, the majority

of lateral smearing occurs in a NW–SE pattern in the west, and in a SW–NE trend in the east. This is due to the preferential raypath directions caused by event-station distributions.

[32] Deeper, a synthetic high-velocity slab-like structure is inserted in the transition zone. This anomaly is resolved, although slightly smeared in both the vertical and horizontal directions. This smearing is due to the decreased sensitivity of the data at depth, and this result is amplified by the increased amount of smoothing at depth that was applied in the inversion.

[33] Overall, the new data set used to create $\overline{\text{NA07}}$ has improved resolving power, particularly in the upper ~ 300 km of the mantle as demonstrated here and with additional resolution tests presented by Bedle [2008]. Below ~ 300 km, some lateral and vertical smearing is observed, as well as diminished velocity amplitudes. The best geographically resolved region of the continent is beneath Texas. This is due to the exceptional cross-cutting relationship of seismic rays in this region as events along the western margin and Central America are recorded by a plethora of east coast and west coast stations, respectively. For the remainder of the North American continent, features on the order of ~ 500 km are well resolved spatially down to and within the transition zone, with exceptions beneath Alaska and Northern Canada. In the transition zone, features smaller than ~ 500 km diameter are not well resolved. The highest resolved regions correlate well with the areas where dense seismic arrays have been employed, such as EarthScope’s USArray Transportable Array in the Western United States, as well as in southern Quebec and Ontario where POLARIS stations are located. The eastward continuation of USArray should drastically improve the amplitude recovery capabilities of tomographic models, as well as allowing for resolution of smaller structures.

5. Discussion

5.1. North American Craton

[34] The world’s largest craton appears underlain by high *S* velocities on an equally large scale. These high velocities,

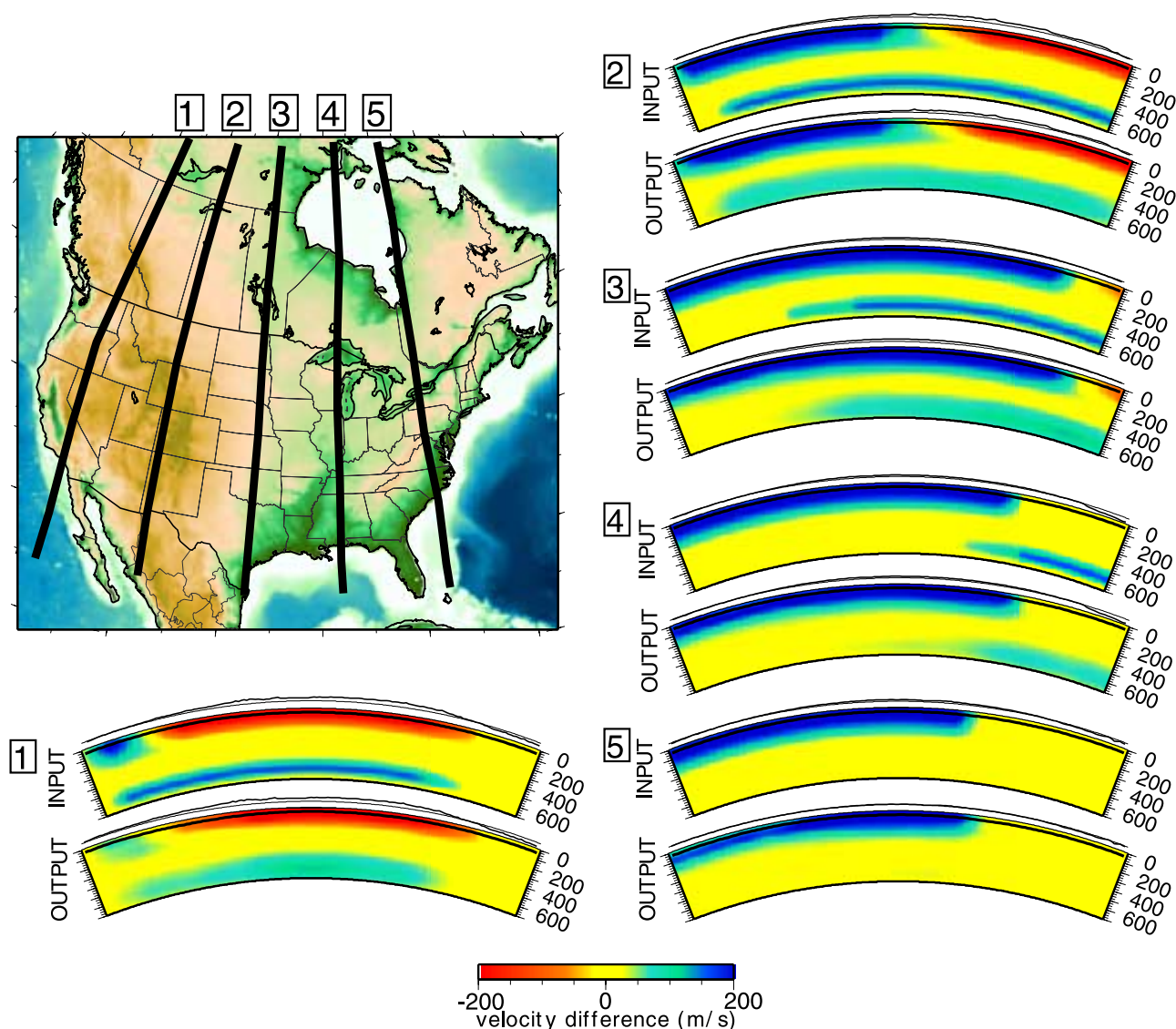


Figure 11. Cross sections through a simplified velocity structure resolution, which demonstrate the resolving power of NA07 parameterization in recovering large-scale velocity anomalies.

which lie beneath the Canadian shield and north central/northeastern United States, are associated with the cool, chemically depleted, thick lithosphere of the North American craton, and extend from the crust to depths of over 250 km (Figure 10). Our modeled depth extent of the cratonic lithosphere agrees with other geophysical studies [Jaupart *et al.*, 1998; Rudnick *et al.*, 1998], as well as results in other regional tomographic studies [Godey *et al.*, 2004; van der Lee and Frederiksen, 2005; Marone *et al.*, 2007].

[35] In NA07, the average cratonic velocities are modeled laterally over the suite range from 4.69 km/s from the Moho to 120 km, 4.63 km/s at 160 km, 4.58 km/s at 200 km, to 4.55 km/s at 250 km with a maximum standard deviation of 0.04 km/s. At 250 km, the anomalies do not extend as far to the west and south as they do in the shallower lithosphere. The deeper velocities are more readily observed beneath Canada, suggesting that the Archean portion of the craton may be thicker than the Proterozoic part. These absolute velocity variations are on the order of those cited by Godey *et al.* [2004] and Goes and van der Lee [2002] who

concluded that down to ~ 230 km, the high velocities of the cratonic roots can be explained by a decrease in temperature, and depletion in iron as compared to the ambient upper mantle. The variation in cratonic velocities within our model suite represent only a fraction of the uncertainty that is introduced when translating velocity anomalies to thermal and compositional variations as quantified by Godey *et al.* [2004]. Using the $d\beta/dT$ relations of Cammarano *et al.* [2003] derived assuming a 1300°C adiabat, the average temperature in the craton at 120 km depth can vary from the average by -277°C if using an iron depletion of 2.5% as found by Godey *et al.* [2004], to -305°C if instead assuming an iron depletion of 1% as calculated by Goes and van der Lee [2002].

[36] The highest cratonic velocities are modeled primarily beneath the Superior craton, but no significant distinctions are modeled between the Archean-age Superior, Hearne, Rae, and Slave cratons. Additionally, NA07 does not model amplitude variations between the different amalgamated portions of the North American craton. One exception to

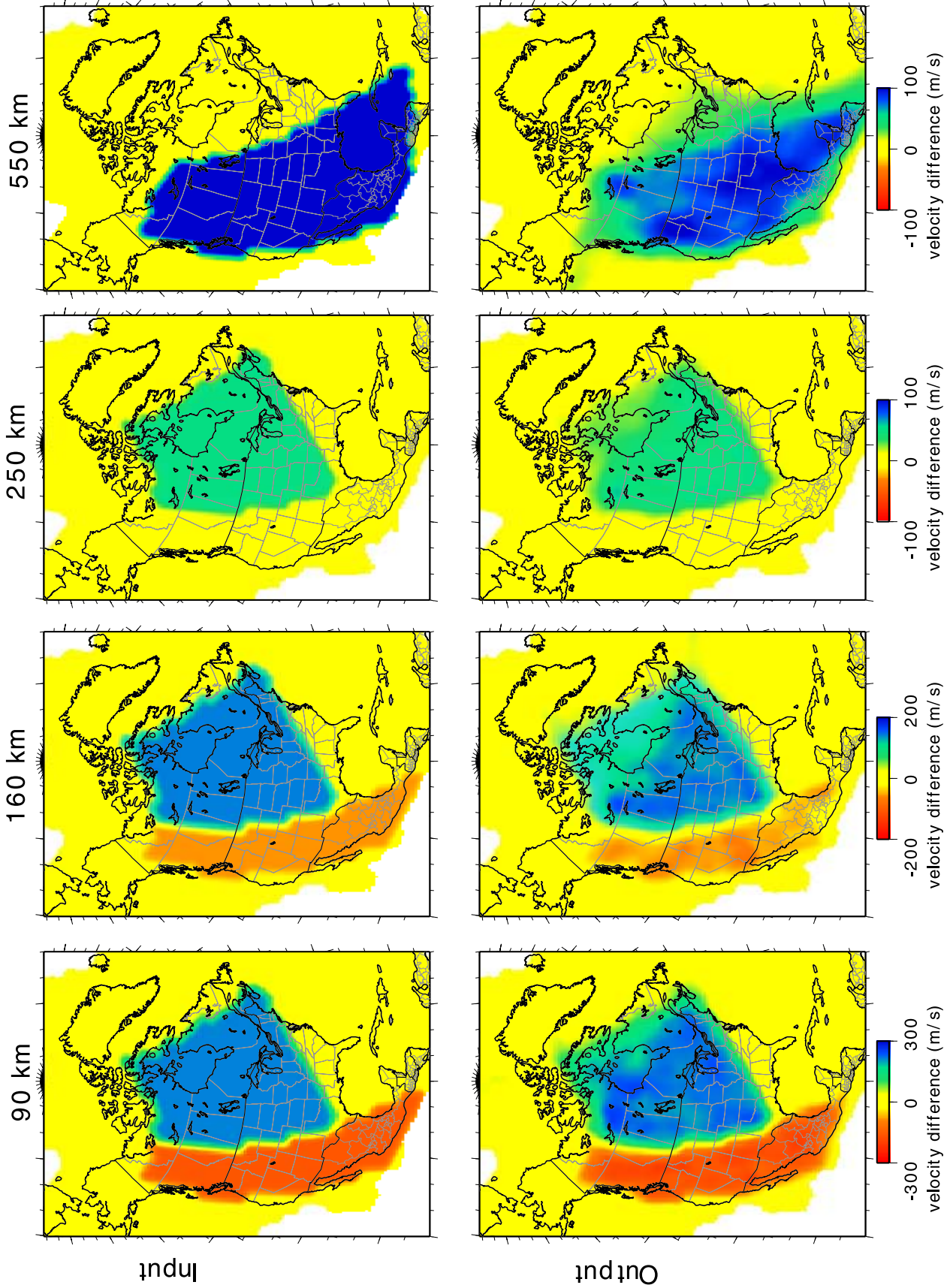


Figure 12. Resolution test for model NA07, inverting for a simplified velocity structure.

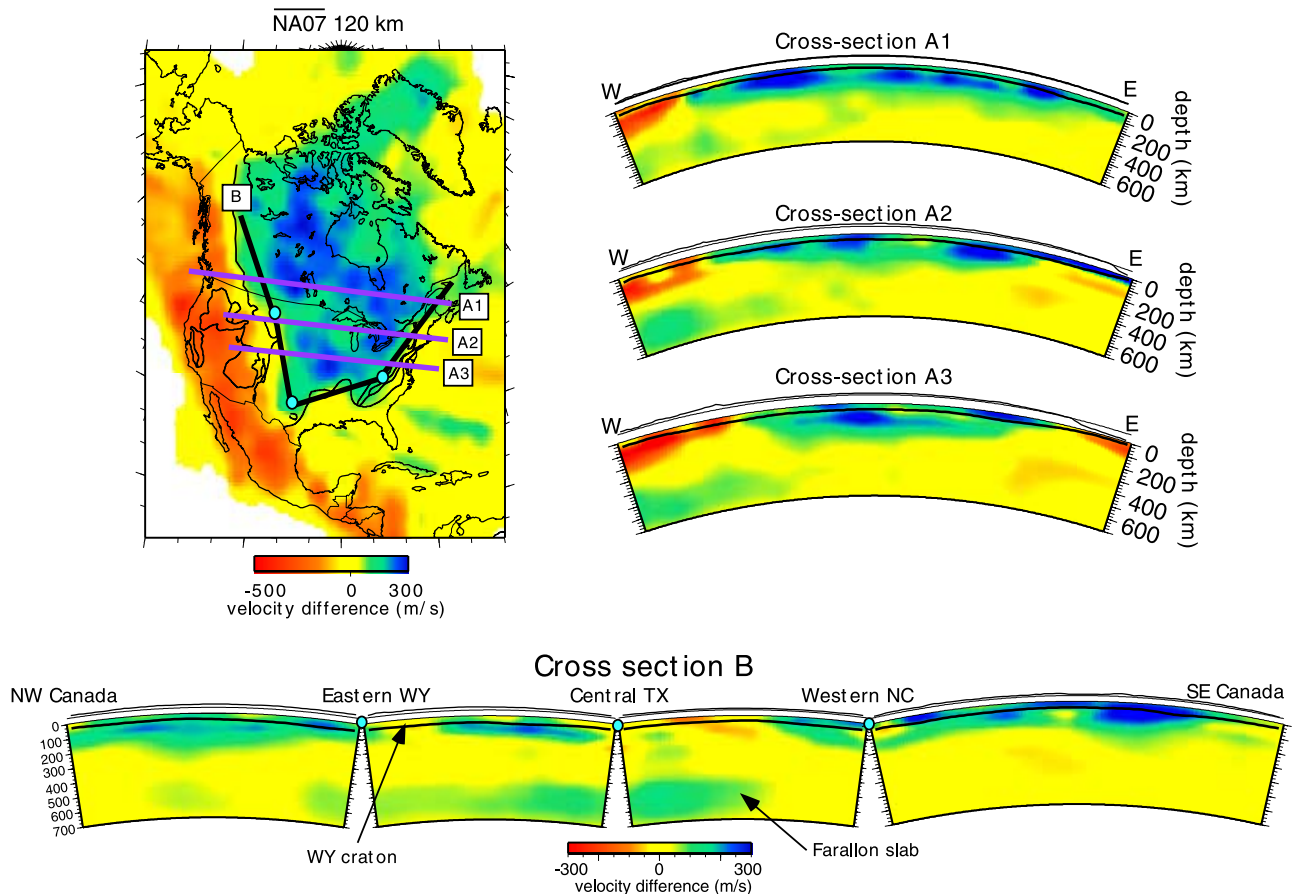


Figure 13. Depth slice through $\overline{\text{NA07}}$ at 120 km shows cross sections A1–A3 transecting the North American craton and cross section B displaying velocities along the edge of the craton.

this is in Greenland, where the Archean Karallan province in the north is geologically and seismically distinct from the Proterozoic lithosphere in southern Greenland (Figure 13). Separating the regions of the craton by age and plotting a one-dimensional average model (Figure 14), these velocity differences between the provinces are clearly observed. The Archean portion of the craton is slightly higher in velocity and thicker than the Proterozoic portion of the North American craton. The Archean lithosphere extends to an average depth of 200 km, although it extends to at least 250 km in some locales as seen in the tomographic images. The Proterozoic craton is on average ~ 175 km thick, and the velocity is ~ 80 m/s lower than the Archean lithosphere. The Archean age Wyoming craton is an exception to the age trend, possessing significantly lower average velocity in the upper 200 km of the upper mantle than other Archean and Proterozoic provinces (Figure 13).

[37] In the western continent, the geographical extent of the transition from the high-velocity craton in the east to the low velocities in the west, appears to vary. North of Wyoming and extending into Canada, the craton transitions at a gradient of $1.8\%/100$ km. To the south, in the western United States, the gradient of the transition is closer to $1\%/100$ km, or less. This can be seen in Figures 13 and 15 particularly below 90 km depth. The southern edge of the craton transitions at a rate of $\sim 0.5\%$ over a region of ~ 100 km, while this slope is slightly steeper at $\sim 1\%/100$ km on the eastern edge of the craton at 120 km depth. Because our data tends to smooth

rather than roughen such large-scale structural transitions, these estimates are underestimates. The actual transitions between the high cratonic velocities and velocities of the surrounding mantle may be much sharper.

[38] This clear-cut eastern margin of the craton is absent in smoother global and regional-scale models [Woodhouse and Dziewonski, 1984; Alsina et al., 1996; Laske and Masters, 1998; Li and Romanowicz, 1996; Grand, 2002; Godey et al., 2003; Zhou et al., 2006; Marone et al., 2007; Nettles and Dziewonski, 2008]. This eastern edge of the seismic craton as modeled in $\overline{\text{NA07}}$, aligns roughly with the edge of the Appalachian orogen (Figure 13). To the south, the craton does not extend south of the Ouachita orogen, and in the west the craton extends to the Rocky Mountain orogen in the United States and Canada. Thus, in model $\overline{\text{NA07}}$, the eastern and southern edges of the craton appear to be defined by the Paleozoic Ouachita–Appalachian orogens related to the formation of Pangaea (Figure 13), rather than the Proterozoic Grenville orogen. These geographical extents of the craton suggest that $\ll 500$ Ma of tectonic stability is needed for craton formation.

5.2. Western Cordillera

[39] Another large-scale seismic feature modeled are the low velocities that underlie most of the western margin of the continent, and which extend east into the continent to the edge of the Rocky Mountain Cordillera. These low velocities beneath the western continent extend from southern Alaska

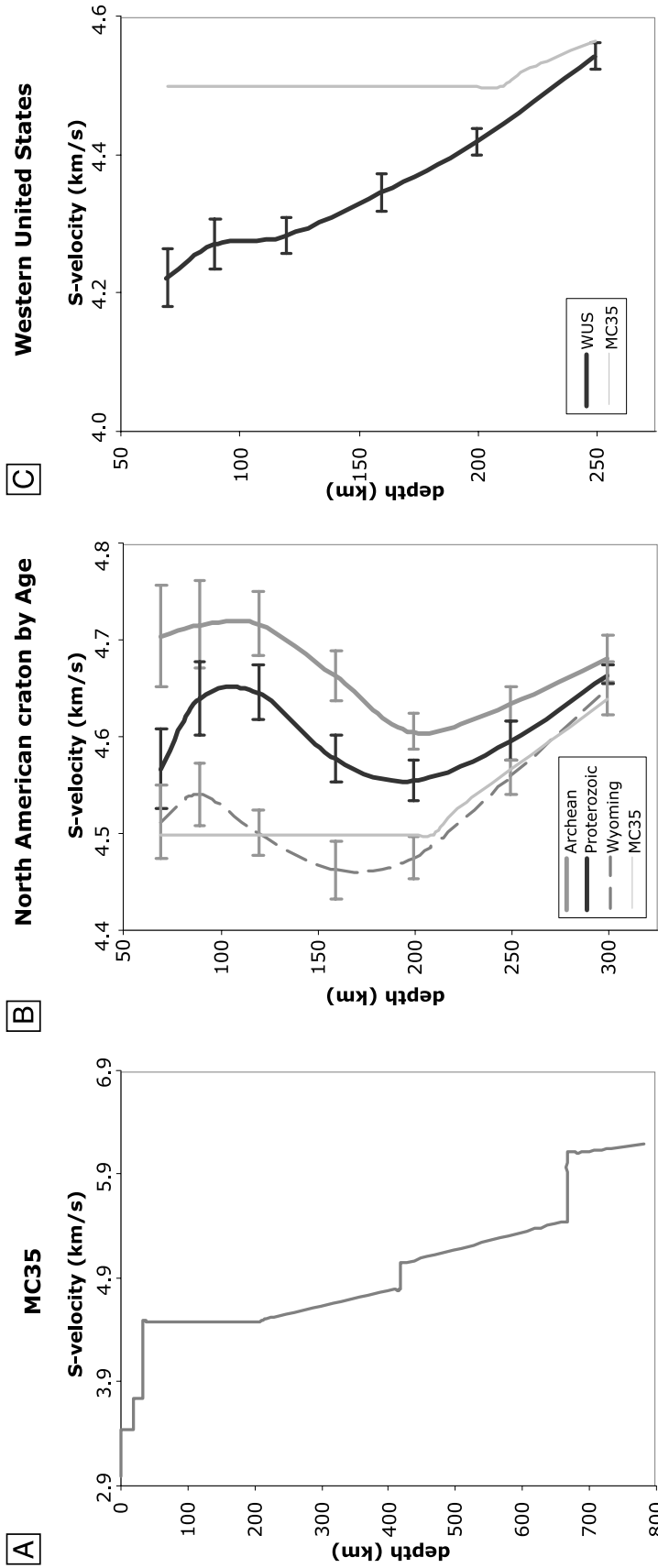


Figure 14. (a) Background model MC35. (b) One-dimensional averaged profiles through the North American craton by age, with error bars marking 1σ . Shown is the average velocity structure for Archean and Proterozoic cratons, as well as an averaged profile through the Archean Wyoming craton, which has lower lithospheric velocity structure than other Archean age provinces. (c) Average velocity profile through the western United States.

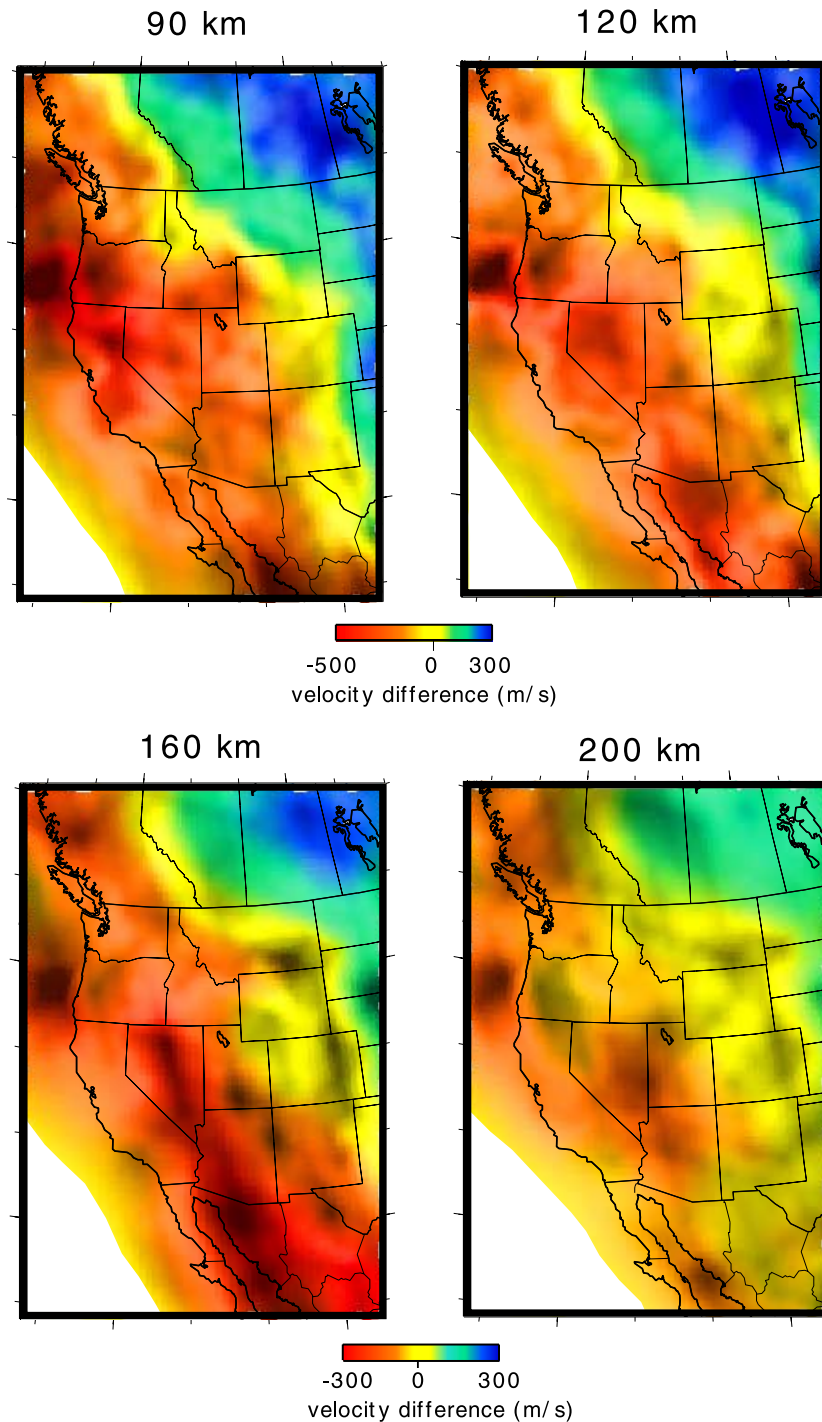


Figure 15. Depth slices through $\overline{\text{NA07}}$, highlighting velocity variations in the western United States at 90, 120, 160, and 200 km depths. Standard deviation is overlain in grey scale, where darker regions represent areas with higher variation in the model suite.

in the north, south into Mexico, terminating in the vicinity of the Pliocene-Quaternary Transmexican Volcanic Belt. This termination of low velocities may be explained by the shallow subduction angle of the Cocos plate in this region, as flat slab subduction could inhibit the hydration of the uppermost mantle, resulting in slightly higher in velocity, but still absolutely low velocity anomalies, or the transition might be related to the higher velocities of the slab itself.

[40] The lowest velocities in this region underlay the Gulf of California, and extend northward beneath the Salton Trough in southern California, down to depths of 160 km. Extremely low velocities are possible in this region as it is an active zone of spreading. $\overline{\text{NA07}}$ models these velocities in the western United States to be on average a -6% S velocity anomaly (Figure 14), although the velocities exceed -12% at shallow mantle depths in some areas. While -6% velocity

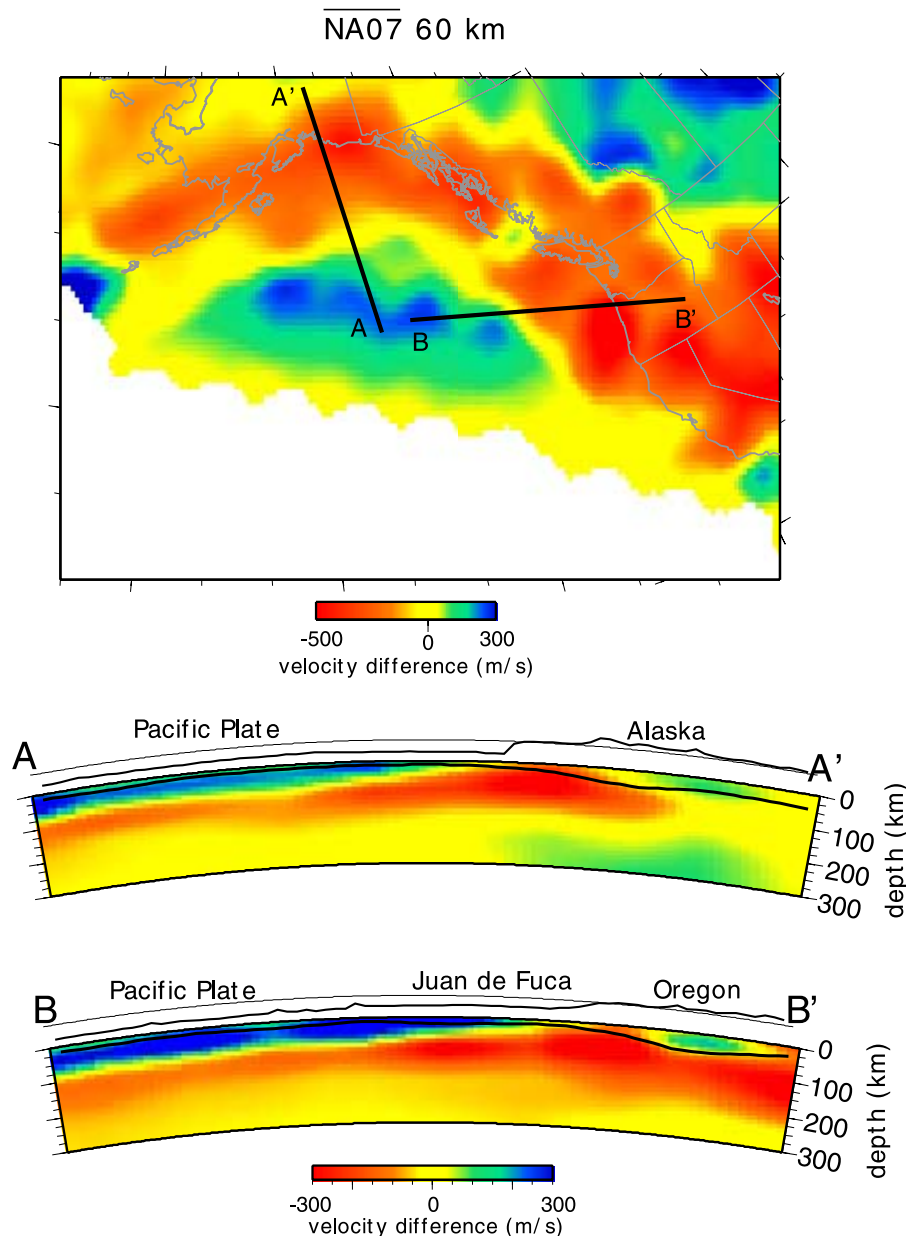


Figure 16. Cross sections through $\overline{\text{NA07}}$, focusing on the thickness of oceanic lithosphere beneath the Pacific Ocean.

anomalies can be reasonably explained with uppermost mantle heated by a few hundreds of degrees, extremes of -12% would require temperature anomalies from 500 to 800°C in this shallow depth range [Cammarano *et al.*, 2003]. While such localized extreme temperature anomalies would elevate the mantle to above the dry solidus, most of the western US (with an average S velocity anomaly of roughly -6%) would be a few hundreds of $^\circ\text{C}$ hotter than the adiabat and thus near the dry solidus but in the solid state if the mantle is dry. Because water lowers the solidus, partial melt would be widespread in the western United States if the uppermost mantle is wet [Dixon *et al.*, 2004]. Extremely low velocities are also modeled off the coast of Oregon and Washington states, corresponding to the Juan de Fuca spreading ridge in the Pacific Ocean.

[41] $\overline{\text{NA07}}$ also shows variations in the seismic velocities of the oceanic lithosphere that are well correlated to the relative age of the plate. The thickness of the oceanic lithosphere beneath the northeast Pacific Ocean off the coast of Alaska (Figure 16) is significantly thicker than the Juan de Fuca plate off the northwest coast of the United States. The lithosphere off the coast of Alaska is close to 40 Ma old and is about ~ 70 km thick. On the other hand, the Juan de Fuca plate shows a much thinner lithosphere, ≤ 20 km, in agreement with its younger age, of about ~ 10 Ma old.

[42] Aside from regions of active spreading, the upper mantle of the western continent has anomalously low velocities. Much discussion has taken place in recent years as to the nature of these low velocities. It has been discussed whether the western United States possesses a thin lithosphere,

underlain by low-velocity Cenozoic mantle [Humphreys and Dueker, 1994; Grand, 1994; Godey et al., 2003]; or, if the uppermost mantle contains a thick, buoyant Proterozoic lithosphere that has been altered in a way so that it seismically resembles the asthenosphere [Karlstrom et al., 2005]. The crux of the latter hypothesis, is that heterogeneities have been imaged in the western US uppermost mantle that correspond to crustal tectonic domains. To get a better look at smaller-scale velocity variations in NA07, Figure 15 plots depths through the western United States portion of model NA07 to help emphasize differences between slow velocity regions.

[43] Figure 15 shows that the western lithosphere has velocity variations on the order of 500 km. These low velocities extend to ~ 200 km, at which depth the strongest velocities are primarily beneath the Basin and Range. Low velocities are also seen at these depths beneath central New Mexico. Overall, few small-scale variations are seen in the western cordillera lithosphere. Resolution tests performed on this model, show that resolution is limited in regards to small-scale features (<300 km), because of the choice of smoothing parameterization and node spacing.

[44] The northern Rocky Mountain region is an area of current research projects which focus on tectonic features such as Juan de Fuca plate subduction, the Newberry and Yellowstone hot spots, as well as being a site of flat slab subduction during the Laramide orogeny. In the Pacific Northwest, NA07 shows the lowest velocities directly below the ocean-continent transition, exceeding -11% . This area is one of the regions with the highest velocity variances. These high standard deviations may likely be related to azimuthal anisotropy bias that is introduced into the model as a function of raypath coverage. In a study done on the 3-D model NA04, Lloyd and van der Lee [2008] found that this region of North America could possess a bias up to ~ 140 m/s at 90 km due to azimuthal anisotropy in the worst case scenario where all anisotropy is confined to the lithosphere. So, it is possible that the low velocities in the Pacific Northwest may be partially attributed to a bias caused by azimuthal anisotropy.

[45] Interestingly, NA07 has high variance in the region of the central Rocky Mountain front (Figure 15, 160 km depth). This suggests that some velocity structure is being imaged in some of the models, and not others. Looking at each individual model in the suite, we find that 40% of the tomographic models image a low-velocity feature extending from New Mexico, northward into central Colorado. The models that imaged this feature all employ a lesser amount of flattening, suggesting that some detail of velocity structures may be lost in model NA07 because of parameterization choices that favored smoother models.

5.3. Midcontinent Illinois Basin

[46] The Illinois basin is an intracratonic sedimentary basin just north of the New Madrid Seismic Zone, which covers parts of Illinois, Indiana, western Kentucky, Tennessee, and Missouri. This basin's uppermost mantle *S* velocity structure differs from that of other North American intracratonic basin, and this anomaly has been addressed in a previous study [Bedle and van der Lee, 2006]. With the additional velocity and crustal constraints added to Bedle and van der Lee's data, NA07 confirms this anomaly. The anomaly now extends from roughly the base of the crust to 85 km, slightly shallower than previously modeled. This

uppermost mantle feature appears robust to within one standard deviation. Bedle and van der Lee [2006] suggested that this uppermost mantle anomaly is related to Proterozoic flat slab subduction.

5.4. Farallon Slab

[47] Model NA04 shows high-velocity anomalies in the transition zone, which have been hypothesized to be related to the subducted Farallon slab. NA07 shows a similar, although broader high-velocity irregularity in the transition zone (Figure 10). This new wide region of high velocities introduces concerns that the PEM-C based 1-D model used as a reference could be too slow in the transition zone. In fact, mineralogical studies prefer a seismically higher velocity in the transition zone for a dry, pyrolytic mantle, than those presented in current seismic 1-D average earth models [Cammarrano et al., 2004, 2005]. The effects of a too-slow reference model were tested by inverting synthetic data for a synthetic structure with a slightly higher velocity (~ 100 m/s) in the transition zone. In the recovered output model, the high velocities are uniformly recovered far north into Canada and past the eastern limits of the continent, well beyond the extent of the high velocities imaged in NA07 [Bedle, 2008].

[48] An inversion was performed using a 1-D model with a 75 m/s faster transition zone compared to the reference model [Bedle, 2008]. The average absolute transition zone velocities from this new inversion are 5.25 km/s, which is only 1% faster than the 5.19 km/s in our reference model, MC35. This difference is not quite equivalent to the 1.5% (75 m/s) difference between the starting 1-D models, suggesting that the reference model does have an effect the tomographic model, particularly in regions with low data sensitivity. Nonetheless, it appears that there is indeed a seismic difference in the transition zone between the western and the easternmost United States. This result agrees with other tomographic regional studies that rely on different methodologies, which have also modeled a high-velocity anomaly in the transition zone beneath the western United States [Marone et al., 2007; Sigloch et al., 2008].

6. Conclusions

[49] Using newly analyzed North American data primarily from the years 2000–2006, a 3-D *S* velocity model was inverted for. This velocity model, HB07, contains data entirely independent of the data in model NA04 [van der Lee and Frederiksen, 2005] and additionally employs different parameterization, including a new grid. Nonetheless, HB07 images similar velocity heterogeneities as NA04, confirming the presence of the previously imaged structures, among them high velocities in the transition zone beneath the western continent.

[50] A three-dimensional *S* velocity model of the upper mantle beneath North America was created from a suite of good-fit models, each created using different parameterization and data subset. This model, NA07, images the depth of the Archean portions of the North American craton at ~ 200 km, while the Proterozoic portion of the craton extends to on average ~ 175 km, and is ~ 80 m/s slower than the Archean portion. One exception to this age trend is the Archean Wyoming craton, which possess a lower average in the upper 200 km of the mantle than the rest of the Archean

and Proterozoic portions of the craton. Overall, the North American craton is roughly 300°C less hot than the average mantle at a depth of 120 km.

[51] The eastern and southern edges of the craton appear to be defined by the Paleozoic Ouachita and Appalachian orogens, as opposed to Proterozoic orogens, suggesting that as little as 500 Ma of tectonic stability is needed for craton formation. The western edge of the craton abuts the western Rocky Mountain cordillera. In Canada and the northernmost United States the transition from the high velocities of the craton edge to 100 m/s lower velocities beneath the western continent occurs over a ~150 km region, while beneath Wyoming and Colorado a similar velocity transition occurs over a much broader (~500 km) region. This broader zone is most likely related to the Laramide episode of flat slab subduction that occurred south of Montana. Low velocities are observed beneath the western continent, extending in the north from southern Alaska into Mexico where the low velocities terminate in the region of the Transmexican Volcanic Belt. These low velocities likely terminate in this region because of the shallow north dipping subduction angle of the Cocos plate.

[52] The lowest velocities in the west are imaged beneath the Gulf of California and extend north to the Salton Trough in California. These extremely low velocities are best explained by a combination of temperature and the presence of partial melts at shallow depths. Beneath the ocean-continent transition in the Pacific northwest, *S* velocity anomalies in $\overline{NA07}$ are also extreme at -11%.

[53] In the transition zone, the addition of new waveform constraints extended the region of high velocities beneath the western continent further to the north and east. On the basis of the results resolution tests and independent models from the literature, it appears that a significant *S* velocity difference indeed exists in the transition zone between the western and eastern continent. These higher velocities in the west are possibly related to the presence of part of the subducted Farallon slab in the transition zone. A smaller region of weakly low *S* velocities beneath the eastern US has been explored by *van der Lee et al.* [2008] and has been associated with an elongated hydrous upwelling with the potential to trigger future subduction of the Atlantic Ocean.

[54] **Acknowledgments.** This work was supported by NSF grant EAR-0346200. Figures 1–4, 7–13, 15, and 16 were drawn using GMT [Wessel and Smith, 1995]. We would also like to acknowledge that our data were collected from the Incorporated Research Institutions for Seismology data management center (<http://www.iris.edu>), and that we used data generously supplied by seismic networks mentioned in Table 1, including data from EarthScope's USArray facility.

References

Aktas, K., and D. W. Eaton (2006), Upper-mantle velocity structure of the lower Great Lakes region, *Tectonophysics*, 420(1–2), 267–281.

Alsina, D., R. Woodward, and R. Snieder (1996), Shear wave velocity structure in North America from large-scale waveform inversions of surface waves, *J. Geophys. Res.*, 101(B7), 15,969–15,986.

Bedle, H. (2008), Studies on the *S*-velocity structure of the North American upper mantle, Ph.D. thesis, Northwestern Univ., Evanston, Ill.

Bedle, H., and S. van der Lee (2006), Fossil flat-slab subduction beneath the Illinois basin, USA, *Tectonophysics*, 424(1–2), 53–68.

Bleeker, W. (2003), The late Archean record: A puzzle in ca. 35 pieces, *Lithos*, 71, 99–134.

Boschi, L., and G. Ekström (2002), New images of the Earth's upper mantle from measurements of surface wave phase velocity anomalies, *J. Geophys. Res.*, 107(B4), 2059, doi:10.1029/2000JB000059.

Bunge, H., and S. Grand (2000), Mesozoic plate-motion history below the northeast Pacific Ocean from seismic images of the subducted Farallon slab, *Nature*, 405(6784), 337–340.

Cammarano, F., S. Goes, P. Vacher, and D. Giardinia (2003), Inferring upper-mantle temperatures from seismic velocities, *Phys. Earth Planet. Inter.*, 138, 222–2197.

Cammarano, F., S. Goes, A. Deuss, and D. Giardinia (2004), Is a pyrolytic adiabatic mantle compatible with seismic data?, *Earth Planet. Sci. Lett.*, 232, 227–243.

Cammarano, F., A. Deuss, S. Goes, and D. Giardini (2005), One-dimensional physical reference models for the upper mantle and transition zone: Combining seismic and mineral physics constraints, *J. Geophys. Res.*, 110, B01306, doi:10.1029/2004JB003272.

Crotwell, H., and T. Owens (2005), Automated receiver function processing, *Seismol. Res. Lett.*, 76, 206–702.

Dixon, J. E., T. H. Dixon, D. R. Bell, and R. Malservisi (2004), Lateral variation in upper mantle viscosity: Role of water, *Earth Planet. Sci. Lett.*, 222, 451–467.

Dziewonski, A., A. Hales, and E. Lapwood (1975), Parametrically simple Earth models consistent with geophysical data, *Phys. Earth Planet. Inter.*, 10(1), 12–48.

Dziewonski, A., A. Friedman, D. Giardini, and J. Woodhouse (1983), Global seismicity of 1982: Centroid-moment tensor solutions for 308 earthquakes, *Phys. Earth Planet. Inter.*, 33, 76–90.

Eaton, D., and A. Frederiksen (2007), Seismic evidence for convection-driven motion of the North American plate, *Nature*, 446, 428–431.

Friederich, W. (2003), The *s*-velocity structure of the east Asian mantle from inversion of shear and surface waveforms, *Geophys. J. Int.*, 153, 88–102.

Gao, W., S. P. Grand, W. S. Baldrige, D. Wilson, M. West, J. F. Ni, and R. Aster (2004), Upper mantle convection beneath the central Rio Grande rift imaged by *P* and *S* wave tomography, *J. Geophys. Res.*, 109, B03305, doi:10.1029/2003JB002743.

Godey, S., R. Snieder, A. Villasenor, and H. Benz (2003), Surface wave tomography of North America and the Caribbean using global and regional broad-band networks: Phase velocity maps and limitations of ray theory, *Geophys. J. Int.*, 152(3), 629–632.

Godey, S., F. Deschamps, J. Trampert, and R. Snieder (2004), Thermal and compositional anomalies beneath the North American continent, *J. Geophys. Res.*, 109, B01308, doi:10.1029/2002JB002263.

Goes, S., and S. van der Lee (2002), Thermal structure of the North American uppermost mantle inferred from seismic tomography, *J. Geophys. Res.*, 107(B3), 2050, doi:10.1029/2000JB000049.

Gorman, A. R., et al. (2002), Deep probe: Imaging the roots of western North America, *Can. J. Earth Sci.*, 39(3), 375–398.

Grand, S. (1994), Mantle shear structure beneath the Americas and surrounding oceans, *J. Geophys. Res.*, 99(6), 11,591–11,621.

Grand, S. (2002), Mantle shear-wave tomography and the fate of subducted slabs, *Philos. Trans. R. Soc. London, Ser. A*, 360(1800), 2475–2491.

Humphreys, E., and K. Dueker (1994), Physical state of the western U.S. mantle, *J. Geophys. Res.*, 99, 9635–9650.

Jaupart, C., J. C. Mareschal, L. Guillou-Frottier, and A. Davaille (1998), Heat flow and thickness of the lithosphere in the Canadian Shield, *J. Geophys. Res.*, 103(B7), 15,269–15,286.

Karlstrom, K., and E. Humphreys (1998), Persistent influence of Proterozoic accretionary boundaries in the tectonic evolution of southwestern North America: Interaction of cratonic grain and mantle modification events, *Rocky Mt. Geol.*, 33(2), 161–179.

Karlstrom, K., et al. (2005), Synthesis of results from the CD-ROM experiment: 4-D image of the lithosphere beneath the Rocky Mountains and implications for understanding the evolution of continental lithosphere, in *The Rocky Mountain Region—An Evolving Lithosphere: Tectonics, Geochemistry, and Geophysics*, *Geophys. Monogr. Ser.*, vol. 154, edited by K. Karlstrom and G. Keller, pp. 421–441, AGU, Washington, D. C.

Laske, G., and G. Masters (1998), Surface-wave polarization data and global anisotropic structure, *Geophys. J. Int.*, 132(2), 508–520.

Lee, C.-T. A. (2003), Compositional variation of density and seismic velocities in natural peridotites at STP conditions: Implications for seismic imaging of compositional heterogeneities in the upper mantle, *J. Geophys. Res.*, 108(B9), 2441, doi:10.1029/2003JB002413.

Lee, D.-K., and S. Grand (1996), Upper mantle shear structure beneath the Colorado Rocky Mountains, *J. Geophys. Res.*, 101(B10), 22,233–22,244.

Levander, A., C. Zelt, and M. B. Magnani (2005), Crust and upper mantle velocity structure of the southern Rocky Mountains from the Jemez Lineament to the Cheyenne Belt, in *The Rocky Mountain Region: An Evolving Lithosphere*, *Geophys. Monogr. Ser.*, vol. 154, edited by K. E. Karlstrom and G. R. Keller, pp. 293–308, AGU, Washington, D. C.

Li, A., D. W. Forsyth, and K. M. Fischer (2003), Shear velocity structure and azimuthal anisotropy beneath eastern North America from Rayleigh

- wave inversion, *J. Geophys. Res.*, 108(B8), 2362, doi:10.1029/2002JB002259.
- Li, X., and B. Romanowicz (1996), Global mantle shear velocity model developed using nonlinear asymptotic coupling theory, *J. Geophys. Res.*, 101(10), 22,245–22,272.
- Ligorria, J. P., and C. J. Ammon (1999), Iterative deconvolution and receiver-function estimation, *Bull. Seismol. Soc. Am.*, 89, 1395–1400.
- Lloyd, S. M., and S. van der Lee (2008), Influence of observed mantle anisotropy on isotropic tomographic models, *Geochem. Geophys. Geosyst.*, 9, Q07007, doi:10.1029/2008GC001997.
- Marone, F., and B. Romanowicz (2007), The depth distribution of azimuthal anisotropy in the continental upper mantle, *Nature*, 447, 198–201.
- Marone, F., Y. Gung, and B. Romanowicz (2007), Three-dimensional radial anisotropic structure of the North American upper mantle from inversion of surface waveform data, *Geophys. J. Int.*, 171, 206–222, doi:10.1111/j.1365-246X.2007.03465.x.
- Menke, W., and V. Levin (2002), Anomalous seaward dip of the lithosphere-asthenosphere boundary beneath northeastern USA detected using differential-array measurements of Rayleigh waves, *Geophys. J. Int.*, 149(2), 413–421.
- Nettles, M., and A. Dziewonski (2008), Radially anisotropic shear velocity structure of the upper mantle globally and beneath North America, *J. Geophys. Res.*, 113, B02303, doi:10.1029/2006JB004819.
- Nolet, G. (1990), Partitioned waveform inversion and two-dimensional structure under the network of autonomously recording seismographs, *J. Geophys. Res.*, 95(6), 8499–8512.
- Paige, C., and M. Saunders (1982), Lsq: Sparse linear equations and least squares problems, *AMC Trans. Math.*, 8(2), 195–209.
- Ritzwoller, M. H., N. M. Shapiro, M. P. Barmin, and A. L. Levshin (2002), Global surface wave diffraction tomography, *J. Geophys. Res.*, 107(B12), 2335, doi:10.1029/2002JB001777.
- Rudnick, R., W. McDonough, and R. O'Connell (1998), Thermal structure, thickness and composition of the continental lithosphere, *Chem. Geol.*, 145, 395–411.
- Schmid, C., S. Goes, S. van der Lee, and D. Giardini (2002), Fate of the Cenozoic Farallon slab from a comparison of kinematic thermal modeling with tomographic images, *Earth Planet. Sci. Lett.*, 204(1–2), 17–32.
- Sigloch, K., N. McQuarrie, and G. Nolet (2008), Two-stage subduction history under North America inferred from multiple-frequency tomography, *Nat. Geosci.*, 1, 458–462, doi:10.1038/ngeo23.
- van der Lee, S. (2002), High-resolution estimates of lithospheric thickness from Missouri to Massachusetts, USA, *Earth Planet. Sci. Lett.*, 203(1), 15–23.
- van der Lee, S., and A. Frederiksen (2005), Surface wave tomography applied to the North American upper mantle, in *Seismic Earth: Array Analysis of Broadband Seismograms*, *Geophys. Monogr. Ser.*, vol. 157, edited by A. Levander and G. Nolet, pp. 67–80, AGU, Washington, D. C.
- van der Lee, S., and G. Nolet (1997), Upper mantle *S* velocity structure of North America, *J. Geophys. Res.*, 102(10), 22,815–22,838.
- van der Lee, S., K. Regenauer-Lieb, S. Jacobsen, and D. Yuen (2008), The role of water in connecting past and future episodes of subduction, *Earth Planet. Sci. Lett.*, 273, 15–27, doi:10.1016/j.epsl.2008.04.041.
- Wessel, P., and W. H. F. Smith (1995), New version of the generic mapping tools released, *Eos Trans. AGU*, 76(33), 329.
- West, M., J. Ni, W. Baldrige, D. Wilson, R. Aster, W. Gao, and S. Grand (2004), Crust and upper mantle shear wave structure of the southwest United States: Implications for rifting and support for high elevation, *J. Geophys. Res.*, 109, B03309, doi:10.1029/2003JB002575.
- Wilson, D., R. Aster, J. Ni, S. Grand, M. West, W. Gao, W. S. Baldrige, and S. Semken (2005), Imaging the seismic structure of the crust and upper mantle beneath the Great Plains, Rio Grande Rift, and Colorado Plateau using receiver functions, *J. Geophys. Res.*, 110, B05306, doi:10.1029/2004JB003492.
- Woodhouse, J., and A. Dziewonski (1984), Mapping the upper mantle: Three-dimensional modeling of earth structure by inversion of seismic waveforms, *J. Geophys. Res.*, 89(B7), 5953–5986.
- Yoshizawa, K., and B. Kennett (2002), Determination of the influence zone for surface wave paths, *Geophys. J. Int.*, 149, 440–453.
- Yuan, H., and K. Dueker (2005), Upper mantle tomographic *V_p* and *V_s* images of the Rocky Mountains in Wyoming, Colorado and New Mexico: Evidence for a thick heterogeneous chemical lithosphere, in *The Rocky Mountain Region: An Evolving Lithosphere*, *Geophys. Monogr. Ser.*, vol. 154, edited by K. E. Karlstrom and G. R. Keller, pp. 329–346, AGU, Washington, D. C.
- Zhou, Y., G. Nolet, F. A. Dahlen, and G. Laske (2006), Global upper-mantle structure from finite-frequency surface-wave tomography, *J. Geophys. Res.*, 111, B04304, doi:10.1029/2005JB003677.
- Zhu, L., and H. Kanamori (2000), Moho depth variation in southern California from teleseismic receiver functions, *J. Geophys. Res.*, 105(2), 2969–2980.

H. Bedle, Chevron North America Exploration and Production Company, 100 Northpark Boulevard, Covington, LA 70433, USA. (hbedle@chevron.com)

S. van der Lee, Department of Earth and Planetary Sciences, Northwestern University, 1850 Campus Drive, Evanston, IL 60208, USA.